THEORY, CHARACTERIZATION AND APPLICATIONS OF INFRARED HYPERBOLIC METAMATERIALS

by

Daniel B. Fullager

A dissertation submitted to the faculty of
The University of North Carolina at Charlotte
in partial fulfillment of the requirements
for the degree of Doctor of Philosophy in
Optical Science and Engineering

Charlotte

2017

Approved by:

_____
Dr. Michael A. Fiddy

_____
Dr. Glenn D. Boreman

_____
Dr. Edward B. Stokes

_____
Dr. Tsing-Hua Her

_____
Dr. Ryan S. Adams

ABSTRACT

DANIEL B. FULLAGER. Theory, characterization and applications of infrared hyperbolic metamaterials. (Under the direction of DR. MICHAEL A. FIDDY)

Hyperbolic Metamaterials (HMMs) are engineered structures capable of supporting light-matter interactions that are not normally observed in naturally occuring material systems. These unusual responses are enabled by an enhancement of the photonic density of states (PDOS) in the material. The PDOS enhancement is a result of deliberately introduced anisotropy via a permittivity sign-change in HMM structures which increases the number and frequency spread of possible wave vectors that propagate in the material. Sub-wavelength structural features allow effective medium theories to be invoked to construct the k-space isofrequency quadratic curves that, for HMMs, result in the k-space isofrequency contour transitioning from being a bounded surface to an unbounded one. Since the PDOS is the integral of the differential volume between k-space contours, unbounded manifolds lead to the implication of an infinite or otherwise drastically enhanced PDOS. Since stored heat can be thought of as a set of non-radiative electromagnetic modes, in this dissertation we demonstrate that HMMs provide an ideal platform to attempt to modify the thermal/IR emissivity of a material. We also show that HMMs provide a platform for broadband plasmonic sensing. The advent of commercial two photon polymerization tools has enabled the rapid production of nano- and microstructures which can be used as scaffolds for directive infrared scatterers. We describe how such directive components can be used to address thermal management needs in vacuum environments in order to maximize radiative thermal transfer. In this context, the fundamental limitations of enhanced spon-

taneous emission due to conjugate impedance matched scatterers are also explored. The HMM/conjugate scatterer system's performance is strongly correlated with the dielectric function of the negative permittivity component of the HMM. In order to fully understand the significance of these engineered materials, we examine in detail the electromagnetic response of one ternary material system, aluminium-doped zinc oxide (AZO), whose tuneable plasma frequency makes it ideal for HMM and thermal transfer applications. This study draws upon first principle calculations from the open literature utilizing a Hubbard-U corrected model for the non-local interaction of charge carriers in AZO crystalline systems. We present the first complete dielectric function of industrially produced AZO samples from DC to 30,000 cm^{-1} and conclude with an assessment of this material's suitability for the applications described.

ACKNOWLEDGMENTS

First, and foremost, I would like to thank Professor Michael ”Mike” Fiddy for taking the time to teach me so much and show me what's possible with time and hard work. Since I was dropped off at his door step, he has ensured that I was financially supported and that I always had goals to achieve. Over our time together my eyes have been opened by visits to the other side of the world, conferences with some of the greatest minds in our field, and a constant supply of optimism. I am a better person than I was when I began this process, and I know that I owe a great deal of that to Mike. He is truly one of the finest examples of a human being I have ever met and I'm not sure if I could ever thank him enough for all he has done for me.

I would like to thank John Hudak for noticing my enthusiasm for working in the clean room and for introducing me to Professor Raphael Tsu as well as all his help with my many endeavors.

I would like to thank Professor Raphael Tsu for being patient with my lack of learnedness. His wisdom is of a special sort, and I feel privileged to have been able to share in it. It is primarily due to my interactions with Professor Tsu that I no longer feel any hesitation in asking questions of experts which has enabled me to make many connections over the years that I might otherwise not have had Professor Tsu and I not met.

I would like to thank Scott Williams for countless invaluable tidbits of technical advice, mechanical help, and for listening when I just need to vent. Scott's experience and knowledge have helped me to remain patient and see the bigger picture at times when I need

reminding that things are the way they are for a reason.

I would like to thank Todd Stoops for inspiring me. At the end of the day it was the music that got me here.

I would like to thank Professor Glenn Boreman for both his reassuring presence and the usage of his IR-VASE. This single instrument has been the cornerstone of most of my experimental work and I will forever be indebted to him for being so generous with his equipment.

Lastly, but perhaps most importantly, I would like to thank Professor Tino Hofmann. He has been a great stand-in adviser, friend, and colleague from the moment we met. His patience for my often times excessive exuberance will always be appreciated. I look forward to our continued collaborations going into the future.

TABLE OF CONTENTS

LIST OF FIGURES ix

LIST OF TABLES xiii

CHAPTER 1: Introduction to Hyperbolic Metamaterials 1

1.1. A Brief History of Metamaterials 1

1.2. Electromagnetic Waves and Uniaxial Crystals 3

1.3. HMM Physics and Theory of Operation 7

CHAPTER 2: Hyperbolic Metamaterial Applications in the Open Literature 16

2.1. HMM Lenses for Super Resolution 16

2.2. Passive Non-reciprocal HMMs 18

2.3. Hyperbolic Metasurfaces 20

2.4. Hypercrystals 22

2.5. HMM Plasmonics 24

CHAPTER 3: Review of Published Data 26

3.1. Epitaxial HMM Fabrication and Characterization 26

3.2. HMM Colimators 43

3.3. Direct Laser Writing 44

3.4. Evanescent Fields and Conjugate Matched Scatterers 53

3.5. Transient Dynamics of Evanescent Fields 61

CHAPTER 4: Aluminium Zinc Oxide 63

4.1. Introduction to Aluminium Zinc Oxide 63

4.2. Ellipsometry Data and Fitting for AZO 67

CHAPTER 5: Summary 77

REFERENCES 82

LIST OF FIGURES

FIGURE 1: Examples of uniaxial metamaterial. A) Multi-layer thin films arranged as a stack or so-called type II HMM B) Wires embedded in some host material, otherwise known as a type I HMM 7

FIGURE 2: Index ellipsoids (also known as isofrequency or k-space contours) for free space and the three cases of uniaxial materials considered herein. A) Index ellipsoid construction for free space or isotropic media (spherical) B) Index ellipsoid for an anisotropic material with all-positive components of the permittivity (ellipsoidal) C) The type I HMM's 'index ellipsoid' is actually a hyperbola of two sheets as a result of the normal component of the permittivity being negative D) The type II HMM's 'index ellipsoid' is also a hyperbola, though of a single sheet, as a result of the two transverse components of the permittivity being negative 12

FIGURE 3: Showing two cases of type II HMM with the transverse permittivity set to two different values. A) HMM with a transverse permittivity of $\varepsilon_r = -0.005$. B) HMM with a transverse permittivity of $\varepsilon_r = -50$. In both cases the normal component of ε_r is set to 1 13

FIGURE 4: Showing two cases of type II HMM with the permittivity normal to the HMM surface set to two different values. A) HMM with a transverse permittivity of $\varepsilon_r = -0.005$. B) HMM with a transverse permittivity of $\varepsilon_r = -50$. In both cases the normal component of ε_r is set to 1 15

FIGURE 5: Schematic depicting the ideal multi-layer configuration of a hyperlens. Note the concentric multi-layer configuration which is unique to this device. 17

FIGURE 6: Figure from [80] showing a simulation of the transmitted field through the asymmetric grating HMM combination 18

FIGURE 7: Figure taken from [2] showing how variation in folded dipole bend angle affects relative phase 20

FIGURE 8: Metasurface enabled flat optics will allow for drastically decreased form factors for optical systems. 21

FIGURE 9: Showing a schematic representation of a hypercrystal. Image taken from [49]. 22

FIGURE 10: Showing a comparison between k-space index ellipsoids for a regular type II HMM (left) and for a photonic hypercrystal made from the same HMM and another homogeneous material. Image taken from [49]. 23

FIGURE 11: Showing a comparison between k-space index ellipsoids for a regular type II HMM (left) and for a photonic hypercrystal made from the same HMM and another homogeneous material. Note the scale is $\log_{10}$ indicating PDOS enhancements on the order of 200. Image taken from [23]. 24

FIGURE 12: Cartoon depicting the notion of a vertically aligned free-carrier concentration gradient allowing for broad band absorption. Note how the long wavlength (red) penetrates the entire stack because the energy of the red photon is below the bandgap of the preceding layers. 25

FIGURE 13: Ellipsometry of bare c-plane sapphire showing the index of refraction (blue) and extinction coefficient (red) from 2 to 40 μm 28

FIGURE 14: Ellipsometry of 16-layer ZnO/GZO HMM showing the index of refraction (blue) and extinction coefficient (red) from 2 to 40 μm 30

FIGURE 15: FTIR of 16-layer ZnO/GZO HMM (red) and bare sapphire (blue) substrate showing reflection (top) and transmission (bottom) from 2 to 22 μm. Y-axis is measured signal intensity relative to a gold mirror reference, x-axis is wavelength in μm. 30

FIGURE 16: FTIR of 16-layer ZnO/GZO HMM and bare sapphire substrate (top) compared to VASE scan (bottom) of 16-layer HMM and sapphire substrate from 2 to 25 μm. Y-axis is measured signal intensity relative to a gold mirror reference for the top graph and calculated reflectance from VASE analysis on the lower graph, x-axis is wavelength in μm 31

FIGURE 17: Showing plot of absorption vs wavelength from 2 to 40 μm determined by subtracting measurements of R and T for angles of incidence of 40-70 degrees 32

FIGURE 18: $2\theta - \omega$ XRD scans of HMM structures showing ZnO (002) peak at approximately 34.5 degrees (left) Photoluminescense of HMM excided by HeCd laser (right) 32

FIGURE 19: EDS plot with superimposed SEM image of HMM surface. Note the zinc particles which dot the surface. These inclusions are incompletely evaporated zinc from the electron beam. 33

FIGURE 20: Two simulation results for the electric field in 16-layer ZnO/GZO HMMs for high and low loss regions of operation. Note the enhancement of the field in the lower picture indicating enhanced transmission of high-k modes 34

FIGURE 21: Normalized transmission plot for 16-layer ZnO/GZO HMM from 30-300 THz (y-axis) as a function of the normalized transverse momentum parameter $\frac{k_x}{k_o}$ (x-axis). 36

FIGURE 22: Showing a plot of the electric field enhancement due to the formation of a surface plasmon resonance (left). Note the incident field to the left is almost invisible due to the dynamic scaling of the E-field range. On the right is a reflection (blue) and transmission (green) plot for the surface plasmon resonance shown on the left. Note the very sharp and narrow dip in the reflection and the nearly perfect absorption which correspond to the angle at which the surface plasmon resonance is a solution to Maxwell's equations 37

FIGURE 23: Showing real and imaginary components used to form the permittivity tensors for the 16-layer ZnO/GZO HMM. X-axis is wavelength in μm. Y-axis is in units of Farads/meter. e_1 and e_2 denote the real and imaginary parts of the dielectric function, respectively. 40

FIGURE 24: FLIR-IR Thermal images of gold diffraction gratings on 16-layer ZnO GZO HMM 42

FIGURE 25: (A) and (C) Experimental (dashed green line) and best-model calculated Ψ data (solid red line) for the monomer IP-Dip (A) and IP-L (C) obtained at $\Phi_a = 65^\circ$. Vertical dash marks in (A) and (C) indicate the oscillator center energies listed in Tab. 1 and Tab. 2 below. (B) and (D) Experimental (dashed green line) and best-model calculated Δ data (solid red line) for IP-Dip (B) and IP-L (D) obtained at $\Phi_a = 65^\circ$. 49

FIGURE 26: Best-model calculated real ($\varepsilon_1(\omega)$) and imaginary ($\varepsilon_2(\omega)$) part of the complex dielectric function $\varepsilon(\omega)$ for IP-Dip are shown in panels (A) and (B), respectively. Similarly, (C) and (D) depict $\varepsilon_1(\omega)$ and $\varepsilon_2(\omega)$ for IP-L. The major contributions to the dispersive behavior of both IP-Dip and IP-L occur between 1000 and 2000 cm^{-1}. The best-model parameters are given in Tab. 1 and Tab. 2. 51

FIGURE 27: Microsphere produced by 3D-DLW in a Nanoscribe Photonic Professional GT system. This structure was produced as part of a study of the intrinsic form birefringence in 3D-DLW structures and is currently being used to generate forthcomming publications. 52

FIGURE 28: Nanowire array produced by 3D-DLW in a Nanoscribe Photonic Professional GT system. Note the tilt of the wires. This structure was produced as part of a study of the intrinsic form birefringence in 3D-DLW structures and is currently being used to generate forthcomming publications. 53

FIGURE 29: WVASE32 Model Geometries depicting the 4-layer model used to characterize SALD AZO samples grown at 250°C on silicon. Notice the inclusion of silicon dioxide at the silicon substrate interface as well as the two layers required to describe AZO rather than a single material layer. 64

FIGURE 30: Experimental data (dashed green) vs extended Drude model (solid red) for three angles of incidence. 66

FIGURE 31: Scaled figure with data kindly provided by the authors of [77] showing the theoretically calculated energy levels of the different absorption mechanisms in AZO crystalline systems. 71

FIGURE 32: Total Density of States plot kindly provided by the authors of [77]. The rightmost x-axis value (0 eV) corresponds to the Fermi level. As the Fermi level is pushed higher and higher into the conduction band according to the Burstein-Moss effect more of the states associated with the various inclusion mechanisms are brough into the conduction band. 72

LIST OF TABLES

TABLE 1: IP-Dip best-fit oscillator parameters 50

TABLE 2: IP-L best-fit oscillator parameters 50

TABLE 3: GenOsc parameters for 250°C samples. The Drude response is captured by ρ, the resistivity and τ, the scattering rate. E_{Tauc} represents the onset of indirect transitions associated with phonon absorption while E_n represents the energy associated with the direct inter band transition. A, E, and Br are the amplitude, center energy, and broadening of Gaussian absorption features. Notice the absense of a definite exciton peak in the imaginary part of the permittivity as shown in Tab. 6. The lack of a sharp narrow peak following the indirect transitions gives clear evidence of non-excitonic shallow donor states. 68

TABLE 4: Reflectance polarization ratio (Ψ) for three angles of incidence (65°, 70°, 75°) for 250°C AZO samples. Dashed green lines indicate experimental data. Red line indicates calculated oscillator model parameters. 69

TABLE 5: Relative optical path difference (Δ) for three angles of incidence (65°, 70°, 75°) for 250°C AZO samples. Dashed green lines indicate experimental data. Red line indicates calculated oscillator model parameters. 75

TABLE 6: Real and Imaginary (log scale) relative permittivities for 250°C AZO samples. Red lines indicate the real part ε_1 while the dashed green lines indicate the imaginary part ε_2. 76

CHAPTER 1: INTRODUCTION TO HYPERBOLIC METAMATERIALS

1.1 A Brief History of Metamaterials

The field of metamaterials often traces its origins back to the notion of a negative index of refraction in a synthetic structure presented by Veselago in 1968 [75]. In this seminal work, Veselago showed using arguments from complex analysis that simultaneously negative values of permittivity (ε) and permeability (μ) allow for a negative index of refraction in what he referred to as "left-handed material" (LHM). The terminology for the LHM referrs to the anomalous refraction theoretically exhibited by a material with a negative index of refraction. It was also shown that LHMs are capable of transferring evanescent modes as propagating waves in the steady-state case. This is a direct result of the simultaneously negative values of ε and μ, which causes amplification rather than attenuation of evanescent fields. It is worth noting for posterity that the notion of utilizing sub-wavelength devices to manipulate electromagnetic waves, however, goes back much further [9, 5]. Veselago's observation was perhaps unrealizable for some time until Sir John Pendry published "Magnetism from conductors and enhanced nonlinear phenomena" in 1999 wherein he detailed a method for creating simultaneously negative permittivity and permeability in an artificial structure made from wires and split ring resonators [54]. The following year, Pendry pointed out that the negative refraction predicted in [1] theoretically allowed for diffraction free imaging via a structure termed a "super lens" [52]. It was later observed by Ravi

Hegde et al in 2011 that the this super-resolution forced one to pay the price of exponentially increased imaging time to acquire a super-resolved image [28]. The lack of an effective demonstration of a perfect lens led many to consider new designs such as the hyperlens and Pendry's "poor man's super lens" [33, 84]. Simultaneous with Pendrys work was that of David Smith. Rather than exclusively focusing on achieving negative index of n = -1, Smith pursued achieving negative refraction, a phenomena which manifests the desired behavior of negative index materials with less stringent criteria shown in Eq. 1. The primed terms represent the real parts of ε and μ respectively, while the double primed terms correspond to the imaginary parts.

$$\mu^{'}\varepsilon^{''} + \varepsilon^{'}\mu^{''} < 0 \tag{1}$$

The ideal platform, according to Smith, to achieve negative refraction (without negative index) is an indefinite medium [62]. An indefinite medium is a material or system in which effective medium theories are used to greatly simplify the analysis required to solve Maxwell's equations. In this work a composite material whose constituents are dispersed or arranged on a scale such that they form characteristic features which are well below the wavelength at which the system is designed to interact with is studied. By averaging the individual material properties as a function of their volumetric contribution the correct and desired optical response is obtained. The 'indefinite' characteristic comes from the fact that the sign of $\tilde{\mu}$ or $\tilde{\varepsilon}$ must differ in at least one of three orthogonal basis directions. In the simple case of a uniaxial material, this leads to fundamental differences in how light-matter interactions can occur.

Another possibility of satisfying inequality (1) which has received significant attention from the RF-metamaterial community is to make the signs of μ'' and ε'' both negative. For waves which proceed forward in time, i.e. of the form $e^{-j\omega t}$ negative values of μ'' and ε'' correspond to a gain in the system. In non-Foster circuits (circuits which violate Foster's Reactance Theorem) the gain is achieved by using negative impedance inverters which are a special configuration of an operational amplifier. The notion of relaxed constraints for achieving negative refraction combined with the technique of using engineered anisotropy to manipulate the light-matter interaction in a material led to what are now called hyperbolic metamaterials [65]. The namesake owes its origins to the shape of the manifold in momentum space which represents all the possible wave vectors in the material: a hyperbola.

1.2 Electromagnetic Waves and Uniaxial Crystals

The physics describing light-matter interaction in crystalline solids provides a sufficient basis to understand the operation of HMMs. Furthermore, our knowledge of crystalline optics is enhanced by the large body of work created by the superlattice community, which contributes information about charge transport and the absorption spectra of very thin films. To begin, we consider the Helmholtz equation solved in a material with a single optic axis (a uniaxial crystal). The optic axis is the direction of propagation in a material which does not cause the polarization to change. The polarization is maintained despite the permittivity varying in one direction because the **E**-field sees an average of the two permittivities as a function of the angle of incidence. This phenomena is discussed in detail in subsequent sections.

As is typical in optics, it is safe here to assume the magnetic permeability of the material is approximately equivalent to that of free space. Throughout this document magnetic response will be neglected unless explicitly mentioned. It is worthwhile to note that we begin with Maxwells equations in point form as shown in equations (2-5) below. The constitutive relationship between **D** and **E** shown in equation (6) is considered for the case where the permittivity is not isotropic and therefore requires representation by a tensor.

$$\nabla \times \mathbf{E} = -\frac{\partial \mathbf{B}}{\partial t} \tag{2}$$

$$\nabla \times \mathbf{H} = \frac{\partial \mathbf{D}}{\partial t} + \mathbf{J} \tag{3}$$

$$\nabla \cdot \mathbf{D} = \rho \tag{4}$$

$$\nabla \cdot \mathbf{B} = 0 \tag{5}$$

$$\tilde{\varepsilon}\mathbf{E} = \mathbf{D} \tag{6}$$

Following the method detailed in [58] we assume that the field quantities vary with the position vector **r** as $e^{-j\mathbf{k}\cdot\mathbf{r}}$ where **k**=k$\hat{\mathbf{u}}$. This results in equations (2) and (3) being transformed into

$$\mathbf{k} \times \mathbf{E} = \omega \mu_o \mathbf{H} \tag{7}$$

$$\mathbf{k} \times \mathbf{H} = -\omega \mathbf{D} \tag{8}$$

Substituting (7) into (8) results in

$$\mathbf{k} \times \mathbf{k} \times \mathbf{E} = -\omega^2 \mu_o \mathbf{D} \tag{9}$$

Substituting (6) into (9) then gives

$$\mathbf{k} \times \mathbf{k} \times \tilde{\varepsilon}^{-1}\mathbf{E} = -\omega^2 \mu_o \mathbf{D} \tag{10}$$

The choice of using the electric displacement current flux density is made for convenience since we know that $\mathbf{D}$ is implicitly orthogonal to $\hat{\mathbf{u}}$ from (8). Using the additional constitutive relationships $\eta = \varepsilon_o \tilde{\varepsilon}^{-1}$, $n = \frac{k}{k_o}$, $k_o = \omega\sqrt{\mu_o \varepsilon_o}$ then obtain the equation for projection of the electric impermeability operating on the displacement current flux density below

$$-\hat{\mathbf{u}} \times (\hat{\mathbf{u}} \times \eta \mathbf{D}) = \frac{1}{n^2}\mathbf{D} \tag{11}$$

We can then re-write (11) in the form of an eigenvalue problem

$$\mathbf{P}_u \eta \mathbf{D} = \frac{1}{n^2}\mathbf{D} \tag{12}$$

Such that $\mathbf{P}_u$ is the projection operator. From (12) we obtain an eigenvalue equation whose eigenvalues are index values in the directions of the normal modes of polarization. In the case of a uniaxial crystal, which is sufficient to describe the electromagnetic interaction in a HMM, the effective index of refraction is a function of the angle formed between k and the optic axis of the material is given by

$$\frac{1}{n^2_{effective}(\theta)} = \frac{cos^2(\theta)}{n_o^2} + \frac{sin^2(\theta)}{n_e^2} \tag{13}$$

With an understanding of the index ellipsoid formulation for uniaxial crystals, we can then turn our attention to obtaining the dispersion relations for the HMM. Substituting (6) into (9) results in the equation needed to determine the dispersion relation between ω and $\mathbf{k}$:

$\omega(k_1,k_2,k_3)$.

$$\mathbf{k}\times\mathbf{k}\times\mathbf{E}=\omega^2\mu_o\tilde{\varepsilon}\mathbf{E} \tag{14}$$

The solution to (14) is three linear homogeneous equations which give the components of **E** and is represented in matrix form as

$$\begin{bmatrix} n_1^2k_o^2-k_2^2-k_3^2 & k_1k_2 & k_1k_3 \\ k_2k_1 & n_2^2k_o^2-k_1^2-k_3^2 & k_2k_3 \\ k_3k_1 & k_3k_2 & n_3^2k_o^2-k_1^2-k_2^2 \end{bmatrix}\begin{bmatrix} E_1 \\ E_2 \\ E_3 \end{bmatrix}=\begin{bmatrix} 0 \\ 0 \\ 0 \end{bmatrix}$$

In a uniaxial crystal $n_1=n_2=n_o$ and $n_3=n_e$ therefore the above matrix simplifies to

$$(k^2-k_o^2n_o^2)\left(\frac{k_1^2+k_2^2}{n_e^2}+\frac{k_3^2}{n_o^2}-k_o^2\right)=0 \tag{15}$$

The grouped terms on the left correspond to free space propagation, therefore we consider only the solution to (15) for the grouped terms on the right. Rewriting, we obtain

$$\frac{k_1^2+k_2^2}{n_e^2}+\frac{k_3^2}{n_o^2}=k_o^2 \tag{16}$$

which is the dispersion relation needed to determine $\omega(k_1,k_2,k_3)$. Equation (16) is normally characteristic of an ellipse. Keeping in mind that for non-magnetic media n =$\sqrt{\varepsilon_r}$, we can replace the n^2 terms with ε_r to obtain the desired result:

$$\frac{k_1^2+k_2^2}{\varepsilon_\perp}+\frac{k_3^2}{\varepsilon_\parallel}=k_o^2 \tag{17}$$

The notions of ordinary vs. extraordinary and parallel vs. perpendicular are interchanged somewhat freely in HMM literature. The convention used in this document follows that of Agranovich used in [1]. The labeling will be oriented such that the optic axis is normal to the surface. This is typical of c-plane wurtzite crystalline materials. In the case of zinc

blende or other more complex crystal classes, care must be taken to ensure that the surface is at a known angle to one of the crystal planes so that the effective material parameters can be determined.

1.3 HMM Physics and Theory of Operation

With a firm understanding of the wave mechanics of uniaxial crystals in mind, we turn our attention to understanding the properties of HMMs and indefinite media. In order to consider an engineered structure or material to be a uniaxial material, there must exist two orthogonal directions in which the material properties are exactly equal and a third direction in which they differ. In the event that all three orthogonal directions have different material properties, the medium is biaxial rather than uniaxial and the previously developed formulae fail to properly describe the system. As such we only consider uniaxial HMMs herein. Two structures which have most frequently been platforms for studies of HMMs are multi-layer thin film stacks and host-matrix-embedded wire arrays.

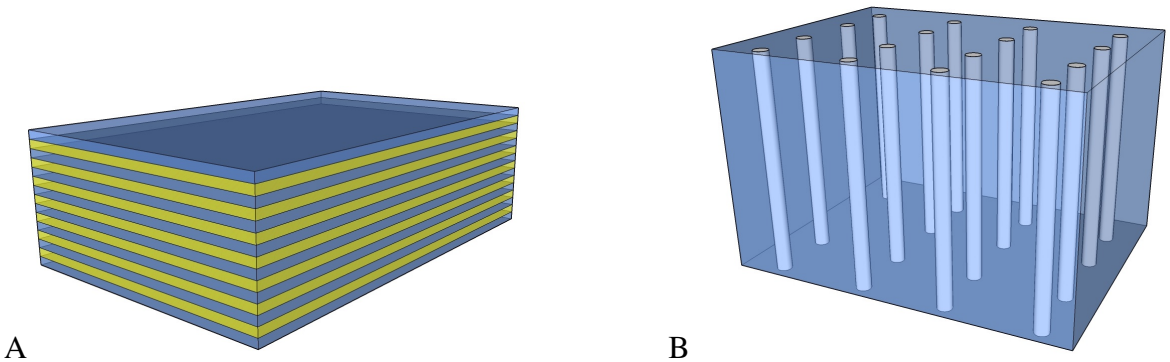

A B

Figure 1: Examples of uniaxial metamaterial. A) Multi-layer thin films arranged as a stack or so-called type II HMM B) Wires embedded in some host material, otherwise known as a type I HMM

In Fig 1 the two most readily realizable variants of uniaxial HMM structures are depicted. Typically it is much easier to fabricate a type II HMM since depositing thin films is a much

more common task than creating an ideally periodic array of uniform wires which are then successfully embedded in some other material. As a result, a majority of the fabrication equipment at most research facilities is more suited to the production of multi-layer HMMs (Fig 1.A). While the analysis is interchangeable from type I to type II, the subsequent discussion in this text often neglects the type I embedded wire configuration for simplicity. Looking at Fig 1.A, let us consider the relevant parameters of the type II HMM. Ultimately we will use (17) to determine the dispersion relationship as previously mentioned. The first question that needs to be addressed, then, is what are the values of $\varepsilon_{\perp}$ and $\varepsilon_{||}$?

The notion of determining an effective crystalline thin film material parameter from multiple constituents with different properties originated in the superlattice community. The effect of having multiple stacked layers of thin film semiconductor is studied in detail in [1] amongst other places. The key results we wish to focus on are the methods for determining the effective bulk material parameters. In equations (19) and (18) below we note there are four parameters of interest. The thickness of the two materials are l_1 and l_2, respectively, and ε_1 and ε_2 are their permittivities.

$$\varepsilon_{\perp} = \frac{\varepsilon_1 l_1 + \varepsilon_2 l_2}{l_1 + l_2} \tag{18}$$

$$\varepsilon_{||} = \left[\frac{1}{l_1 + l_2} \left(\frac{l_1}{\varepsilon_1} + \frac{l_2}{\varepsilon_2} \right) \right]^{-1} \tag{19}$$

Now that we have the ability to **create** the permittivity we want from the materials we have, we might think ourselves ready to jump into designing devices etc. However, often times we will wish to make our type II HMM out of materials which are themselves anisotropic. When this happens there is an extra step involved in using (19) and (18) to

determine (17). Luckily the analysis for a uniaxial metamaterial made from uniaxial crystalline constituents is identical. We then remove the added complexity by iterating through the determination of (13) for each material and then combining parameters using the previously described method. This notion of 'bootstrapping' the effective permittivity can also be applied to HMMs with more than two constituents by a similar iterative process. Equation (20) below shows equation (17) used in conjunction with (18) and (19) to derive an expression for the permittivity as a function of angle from the surface normal.

$$\varepsilon(\theta) = \left[\frac{cos^2(\theta)}{\frac{1}{2}\left(\frac{cos^2(\theta)}{\varepsilon_{1O}} + \frac{sin^2(\theta)}{\varepsilon_{1E}}\right) + \frac{1}{2}\left(\frac{cos^2(\theta)}{\varepsilon_{2O}} + \frac{sin^2(\theta)}{\varepsilon_{2E}}\right)} + \frac{sin^2(\theta)}{\frac{2\left(\frac{cos^2(\theta)}{\varepsilon_{1O}} + \frac{sin^2(\theta)}{\varepsilon_{1E}}\right)^{-1} \times \left(\frac{cos^2(\theta)}{\varepsilon_{2O}} + \frac{sin^2(\theta)}{\varepsilon_{2E}}\right)^{-1}}{\left(\frac{cos^2(\theta)}{\varepsilon_{1O}} + \frac{sin^2(\theta)}{\varepsilon_{1E}}\right)^{-1} + \left(\frac{cos^2(\theta)}{\varepsilon_{2O}} + \frac{sin^2(\theta)}{\varepsilon_{2E}}\right)^{-1}}} \right]^{-1} \tag{20}$$

Establishing the condition that the critical period (the thickness of the layers in the case of multi-layer HMMs) determines the maximum range of wave vectors which are well described by (17) according to the relationship $k_{max} \propto \frac{1}{t_{bi-layer}}$. This limitation is important because it imposes a boundary on the domain of (17) which prevents the photonic density of states from diverging.

The photonic density of states (PDOS) is the number of modes available in a medium to which an EM wave can couple. The PDOS directly relates to the spontaneous emission lifetime via Fermis golden rule [56]. A numerical value for the PDOS in a material or structure can be deduced by integrating the differential volume between isofrequency surfaces over all frequency. The ability to tune the density of states in a material by engineering the ω vs. k dispersion through the proper choice of materials and device configuration thus leads

to the ability to engineer radiative decay rates and emission lifetimes. The usefulness of an enhanced PDOS in a HMM is limited by the ability to access the high-k modes (HKMs) by coupling power into and then out of a given mode. There may also be a potential for an exchange of energy between HKMs which could lead to parametric effects. Initially, it was shown that it was possible to couple the radiation from fluorescent materials into HMMs in order to modify their fluorescence decay rates [36]. However, these modes are sometimes referred to as dark modes as they do not typically re-radiate due to the lack of momentum conservation at the boundary between a material that supports HKMs and a normal medium [37].

For a wave to propagate out of a HMM the standard boundary conditions (22-25) from which we derive Fresnels equations are applied. It is instructive to consider the case of the vector Helmholtz operator acting on **E** (21) to examine the behavior at HMM boundaries for the case of an inhomogeneous solution in this case. The model for the HMM is a sheet of infinite extent whose material properties are only dependent on the angle formed between the surface normal and the incident wave's **k**-vector.

$$\nabla^2\mathbf{E}+\mathbf{k}^2\mathbf{E}=\mu_o\frac{\partial\mathbf{J}}{\partial t} \tag{21}$$

$$\hat{n}\times(\mathbf{E}_1-\mathbf{E}_2)=0 \tag{22}$$

$$\hat{n}\times(\mathbf{H}_1-\mathbf{H}_2)=\mathbf{J} \tag{23}$$

$$(\mathbf{D}_1-\mathbf{D}_2)\cdot\hat{n}=\rho_{bound} \tag{24}$$

$$(\mathbf{B}_1-\mathbf{B}_2)\cdot\hat{n}=0 \tag{25}$$

To obtain a valid solution for (21) it can be seen that (22) must be satisfied at the boundary of interest. As such, the transverse components of **E** must be exactly equal. We can then show that $\mathbf{k} \propto \mathbf{E}$ in order to deduce that the transverse momentum at the HMM-to-isotropic boundary can only differ by a factor of $\mu_o \mathbf{J}$. Since the value of μ_o is $4\pi \times 10^{-7}$ H/m this difference is only significant for weak fields or large surface current densities. A similar argument for the necessary continuity of the **k**-vector at the HMM interface can be made using Snells law. Using the argument that phase matching must occur at the boundary such that the wave is continuously defined, it becomes implicit that $k_o \sin(\theta_i) = k \sin(\theta_t)$. It is critical to remember that this relationship fails to hold for rays in the case where **D** is not parallel to **E** as can be the case in a uniaxial material where the incident wave is not normal to the optic axis. Thus, while we can see an equivalence between wave fronts and rays, the interactions that take place in HMMs are best determined by solving Maxwell's equations. As we have obtained an equation for the k-space surface and the relationship between k-space surfaces of different media for propagating waves we can then graphically represent momentum exchange in HMMs.

Considering equation (17) for the case of free space, we obtain the familiar shape of a sphere since free space is anisotropic, i.e. all the permittivity components are unity as shown in Fig 2.A. Adding some discrepancy between one component of permittivity and the remaining two leads to the ellipsoidal shape of Fig 2.B. Again adding more differentiation to an individual component of the permittivity we then consider the case where one of the components is different and negative. This is the necessary condition to obtain a type I HMM from a uniaxial structure. The direction in which this component is negative for

the case of the type I HMM must be along the optic axis. The consequence is an index ellipsoid which is a surface of two sheets as can be see in Fig 2.C. The final case accounts for when the two components of the permittivity orthogonal to the optic axis are negative and the component normal to the optic axis is positive. This is a type II HMM which has an iso-frequency contour of a single sheet shown in 2.D.

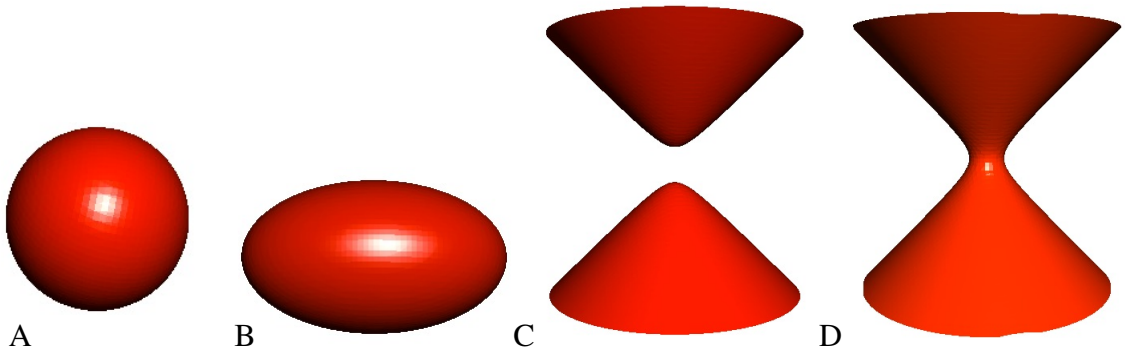

Figure 2: Index ellipsoids (also known as isofrequency or k-space contours) for free space and the three cases of uniaxial materials considered herein. A) Index ellipsoid construction for free space or isotropic media (spherical) B) Index ellipsoid for an anisotropic material with all-positive components of the permittivity (ellipsoidal) C) The type I HMM's 'index ellipsoid' is actually a hyperbola of two sheets as a result of the normal component of the permittivity being negative D) The type II HMM's 'index ellipsoid' is also a hyperbola, though of a single sheet, as a result of the two transverse components of the permittivity being negative

Having obtained the necessary manifolds to perform the vector projection from one index ellipsoid to the other, we can then determine the electromagnetic interaction between two regions with differing material properties. For the sake of simplicity one can also leverage the implicit two coordinate symmetry of the uniaxial HMM index ellipsoid by considering two dimensional cases which are appropriate for any given plane of incidence. There are several special cases of index ellipsoid projection which are worthwhile to consider, as they give interesting and sometimes unexpected results.

For a type II HMM seen in Fig 2.D, the curvature of the index ellipsoid is a function of the permittivity components that are orthogonal to the optic axis. As the values of the transverse permittivity approach zero the hyperbola begins to resemble two parallel planes as shown in Fig3.A with the transverse permittivity set to $\varepsilon_r = -0.005$. As the values approach $-\infty$, the hyperbola approaches the geometry of a cylinder as shown in Fig3.B with the transverse permittivity set to $\varepsilon_r = -50$. The implicit ability to engineer the curvature of the index ellipsoid by choosing the right materials and volume fractions thereof by using Eqn 18 and Eqn 19 allows for the arbitrary selection of wave vectors with which an HMM can interact. This wave vector selectivity then becomes a function of the angle of incidence from the surface normal, leading to the ability to direct outward propagation from a HMM. This is one of the most important traits of HMM and is not seen in any other type of metamaterial.

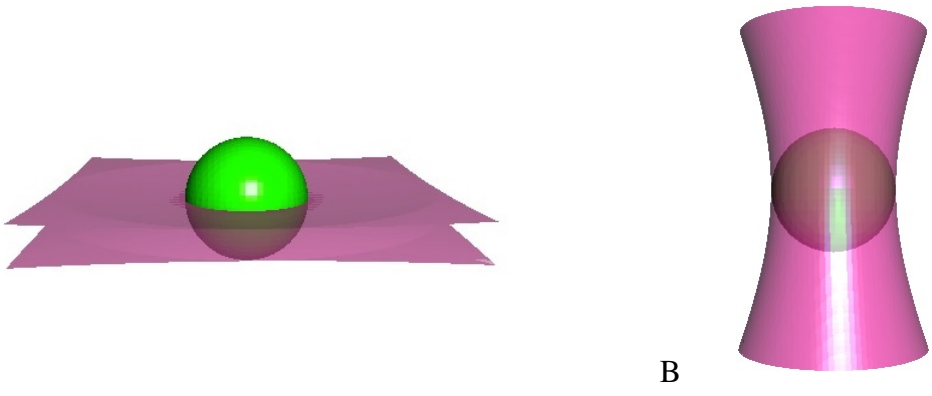

A B

Figure 3: Showing two cases of type II HMM with the transverse permittivity set to two different values. A) HMM with a transverse permittivity of $\varepsilon_r = -0.005$. B) HMM with a transverse permittivity of $\varepsilon_r = -50$. In both cases the normal component of ε_r is set to 1

Analogous to the preceding methodology, one can also consider the effect of varying the normal component of the permittivity on the index ellipsoid electrodynamics for the type II

HMM. The effect of changing the permittivity in the normal direction is a variation in the waist of the type II index ellipsoid. Let us again consider the case of a HMM-to-free space boundary where the normal component of the permittivity is set to $\varepsilon_r = 0.5$ as shown in Fig 4.A. Here we see that the waist of the HMM is actually more narrow than that of free space. While permittivity is typically greater than unity, our ability to invoke Eqn 19 allows us to freely **create** any value we choose provided the necessary material parameters are within reason. One will also note that there is an intersection between the index ellipsoids of free space and a hypothetical HMM shown in Fig 4.A . It is then easy to visualize how one can select materials and fill fractions at a given frequency which create an arbitrary angle at which the HMM transitions from being reflective to transmissive. Similarly, we are free to increase the waist of the index ellipsoid such that the HMM is reflective at all angles for all frequencies. The dispersion in the HMM, then, near a region where we have chosen specific angles at which radiation in or out of the HMM is desired, dictates the rate at which the angular selectivity will vary from the intended device profile.

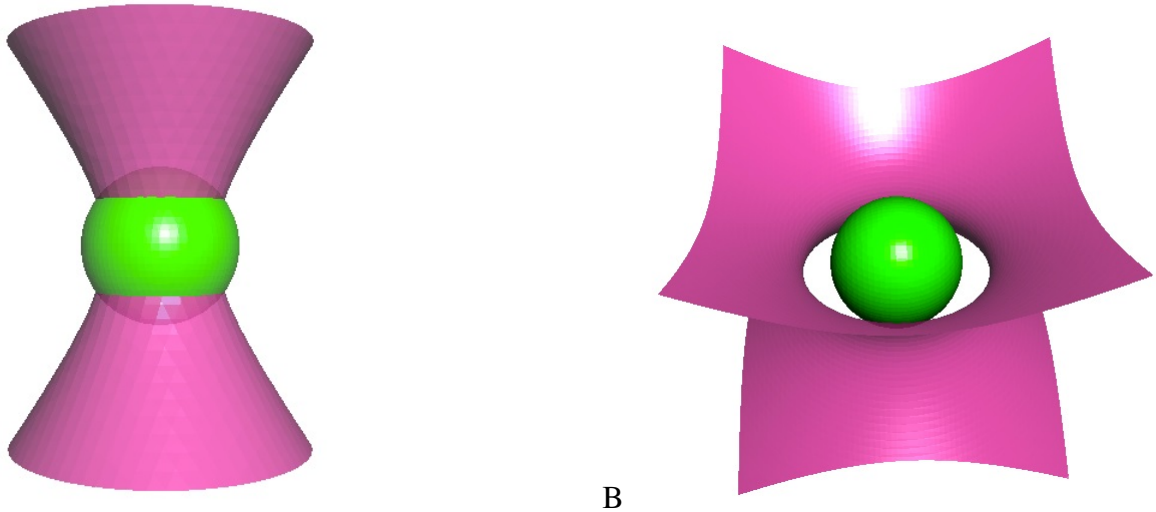

A B

Figure 4: Showing two cases of type II HMM with the permittivity normal to the HMM surface set to two different values. A) HMM with a transverse permittivity of $\varepsilon_r = -0.005$. B) HMM with a transverse permittivity of $\varepsilon_r = -50$. In both cases the normal component of ε_r is set to 1

CHAPTER 2: HYPERBOLIC METAMATERIAL APPLICATIONS IN THE OPEN LITERATURE

2.1 HMM Lenses for Super Resolution

The so-called 'hyperlens' traces its origins to the birth of metamaterial. When the initial attempts at achieving negative index super resolution did not live up to the theoretical predictions, the analysis of indefinite media led to the conclusion that high spatial frequency information could be transferred via hyperbolic dispersion [33]. The important feature of a hyper lens which distinguishes it as a unique application is the radial geometry which allows for the support of spherical modes. Using the plane wave expansion

$$e^{ikr} = \sum_{n=-\infty}^{n=\infty} i^n J_n(kr) e^{in\phi} \tag{26}$$

any plane wave can be decomposed into an infinite series of Bessel functions with independent phase. The high-k modes supported by HMMs are then analogous to the higher order Bessel function terms of the series expansion. The task of super resolution, then, can be though of as recovering the amplitudes and phases of the spherical modes and then reconstructing the plane wave which corresponds to the far field image. It is shown in [35] and elsewhere that the allowed modal structure in a normal cylinder only includes the first few Bessel terms. With the analysis provided in section 1.2 one can infer that the effective medium equations 18 and 19 easily translate to the cylindrical coordinate symmetry

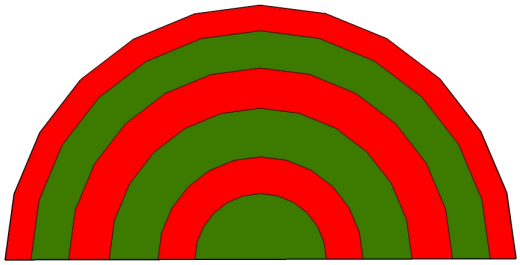

Figure 5: Schematic depicting the ideal multi-layer configuration of a hyperlens. Note the concentric multi-layer configuration which is unique to this device.

provided by 5 which yields

$$\varepsilon_\phi = \frac{\varepsilon_1 l_1 + \varepsilon_2 l_2}{l_1 + l_2} \tag{27}$$

$$\varepsilon_r = \left[\frac{1}{l_1 + l_2} \left(\frac{l_1}{\varepsilon_1} + \frac{l_2}{\varepsilon_2} \right) \right]^{-1} \tag{28}$$

In the regions where the signs of Eqns 27 and 28 differ the structure exhibits the predicted hyperbolic dispersion and acts to transfer high momentum waves at the center of the lens towards its edge which simultaneously causes magnification. This effect has been demonstrated but the range at which 'far field' images can be obtained is in fact rather limited. Due to the necessarily compact size of the imaging system, the volume with which the hyperlens device can interact is implicitly quite small.

2.2 Passive Non-reciprocal HMMs

The notion of violating Helmholtz reciprocity has existed for some time, but has always relied on active devices. Recently, Xu and Lezec showed that sub wavelength gratings coupled to HMMs could be used to engineer the conversion from propagating mode to evanescent mode back to propagating mode to evanescent mode [80]. The drawback to their method was that the choice of materials implicitly lacked ideal crystallinity and showed high loss even in the transmitting direction.

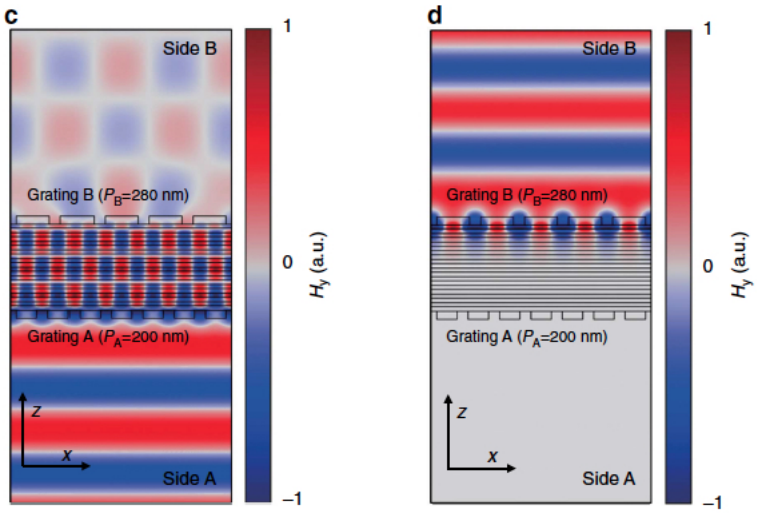

Figure 6: Figure from [80] showing a simulation of the transmitted field through the asymmetric grating HMM combination

The non reciprocity is achieved by the use of a pair of sub wavelength gratings that are coupled to a HMM. The gratings serve to transfer momentum from propagating waves into evanescent modes which are supported in the HMM according to Eqn 29. The reverse process takes place at the back side of the structure but with one difference: the momentum exchange at the second grating is not identical to the process that takes place at the first grating because the gratings are non symmetric. This symmetry breaking in the propagating

to evanescent conversion process leads to the non reciprocal effect.

While the loss is somewhat high, the potential for systems configured in such a manner leads to a large number of applications such as true one way mirrors, passive optical isolators, optical damage protection, and more. An issue that must be immediately overcome with respect to this application is the choice of grating material. While metallic sub wavelength gratings give the desired dispersion for transfer of evanescent modes in HMMs, they also suffer from a large impedance value. This impedance mismatch that is an intrinsic property of the grating leads us to seek other more efficient mechanisms to couple to/from HMMs.

2.3 Hyperbolic Metasurfaces

While the notion of metasurfaces goes back to the concept of geometric phase, or Pancharatnam-Berry phase, the recent interest in sub wavelength electromagnetic devices created by the metamaterials community has led to significant work in the area of metasurfaces. One of the most notable figures working towards better understanding of the engineering of metasurface components is Prof. Federico Capasso. Capasso's group first presented the notion of using an array of sub wavelength folded dipole antennae to arbitrarily alter the phase of a wave front from 0 to 2π to achieve the effects of conventional optics with flat surfaces [2].

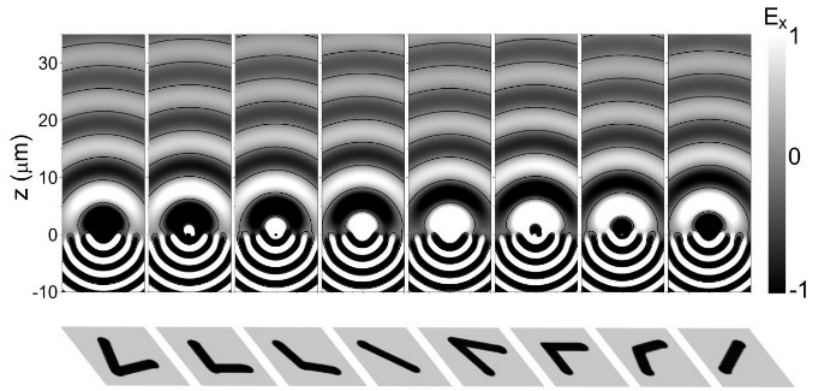

Figure 7: Figure taken from [2] showing how variation in folded dipole bend angle affects relative phase

Flat optics have the advantage of reduced weight as well as reduced degrees of freedom in fabrication. So while a metasurface designed to replace a conventional optical element may be comprised of very fine features, it does not suffer from the complexity of characterization inherent to free form optics. As free form optics is a rapidly growing sub-field of optical engineering, the ability to produce metasurfaces with figures of merit that compete with conventional optics opens a new market. There also exists the potential to retro fit

existing technology with metasurfaces in order to decrease the weight of existing imaging systems. For example, consider Fig 8. One can easily imagine how reducing the form factor of a heavy telephoto lens to that of a single properly patterned silicon-on-insulator wafer would offer incomparable advantages in optical design.

Figure 8: Metasurface enabled flat optics will allow for drastically decreased form factors for optical systems.

Not all metasurfaces are plasmonic. One of the first researchers in the area of metasurfaces, Prof. Erez Hasman, has produced results where he achieves interaction between a metasurface and a laser which shows nearly 100% efficiency [50]. These polaritonic based devices have a much greater device potential as the optical phonon resonances in solid state materials drastically outweigh the electrical resonances leading to large positive permittivity values at certain bandwidths [63]. There is also a growing consensus that dielectric Mie resonators provide an avenue for low loss directive metasurface components [73, 72].

2.4 Hypercrystals

As previously mentioned, the field of metamaterial research began due to the lack of a desired material response from naturally occuring materials. The design space of a typical uniaxial HMM is essentially limited to a choice of frequency/bandwidth, choice of constituent materials, and choice of spatial allocation/material fill fraction. While to most this leaves an endless combination of possibilities and different material science and fabrication challenges, the theoretician will always find a new degree of freedom which in the case of HMMs is a hypercrystal.

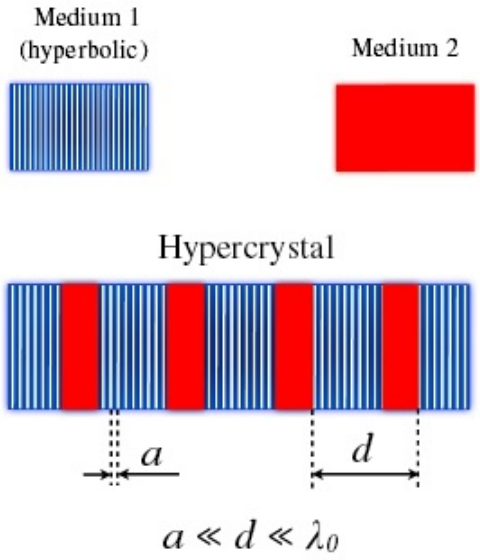

Figure 9: Showing a schematic representation of a hypercrystal. Image taken from [49].

Having developed in detail the necessary formulations to derive the k-space index ellipsoids for HMMs, we observe that the only way to access the enhanced PDOS in many cases is to use a grating or a dielectric cap layer and a specific angle of incidence to couple to high-k modes. In [31] this limitation is discussed and a method to overcome the fixed shape of the iso frequency contours in k-space is detailed. Combining the salient features

of HMMs with 1D photonic crystals, one can superimpose the k-space properties of photonic crystals onto those of HMMs provided certain geometrical restrictions on the spatial period of the individual feature sizes are met.

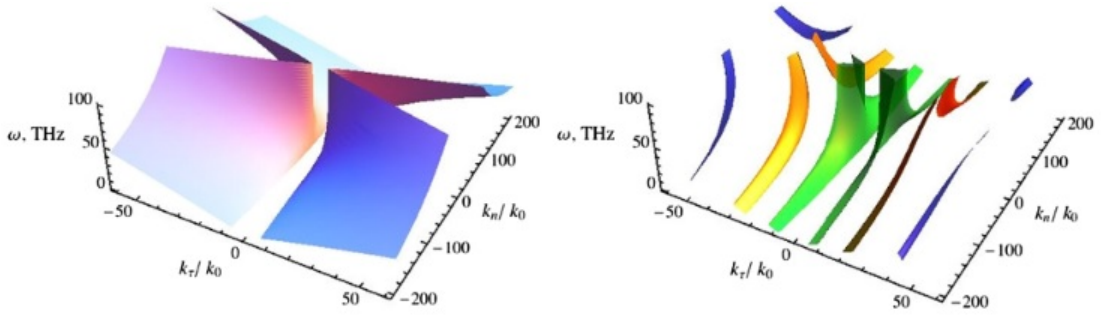

Figure 10: Showing a comparison between k-space index ellipsoids for a regular type II HMM (left) and for a photonic hypercrystal made from the same HMM and another homogeneous material. Image taken from [49].

The photonic hypercrystal is a new idea championed by Prof. Evgenii E. Narimanov, one of the leading contributors in the field of HMMs. It is unique in that it is an amalgamation of two previously existing photonic devices which work as a result of different physical phenomena. HMM response is a function of material choice and fill fraction which is all well described within the effective medium limit. Photonic crystal response is a direct consequence of Bragg scattering and the size scale of 1D photonic crystal elements approaches the effective medium limit.

In [23] Fig. 11 the previously discussed difficulty in out-coupling is overcome via coupling to the spatial features of the photonic crystal component of the hypercrystal.

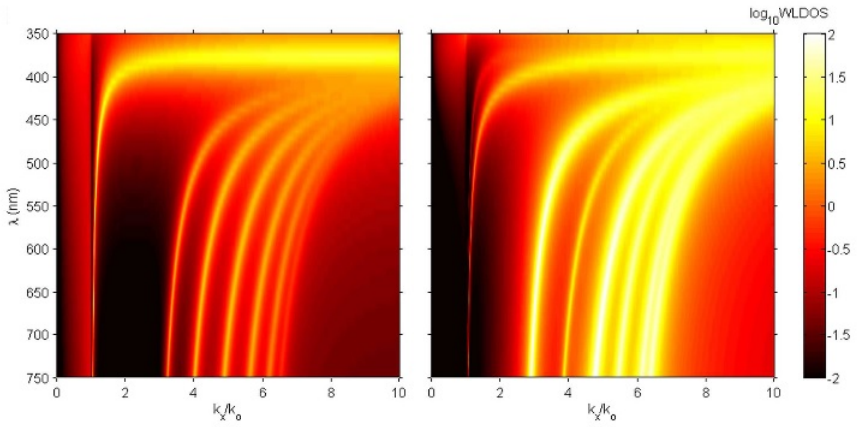

Figure 11: Showing a comparison between k-space index ellipsoids for a regular type II HMM (left) and for a photonic hypercrystal made from the same HMM and another homogeneous material. Note the scale is $\log_{10}$ indicating PDOS enhancements on the order of 200. Image taken from [23].

2.5 HMM Plasmonics

With regards to research in electromagnetism, the only topic to recently receive as much or more attention than metamaterials in the recent past is plasmonics. Invigorated by the pressing need for miniaturizing computing hardware, improved sensing, and better EM devices, plasmonics has been revitalized by technological advances in near field optical microscopy and nanoscale fabrication techniques. Interestingly enough, the notions of plasmonic sensors and hyperbolic metamaterials need not be mutually exclusive of each other.

One of the challenges of coupling photons to electrons in order to form a surface plasmon polariton is the aforementioned problem in coupling to the high-k modes on the surface plasmon polariton dispersion curve which correspond to strongly confined modes stored at the same frequency as the incident radiation in an electron oscillation whose spatial period decreases with increasing transverse momentum. As discussed, a similar problem exists

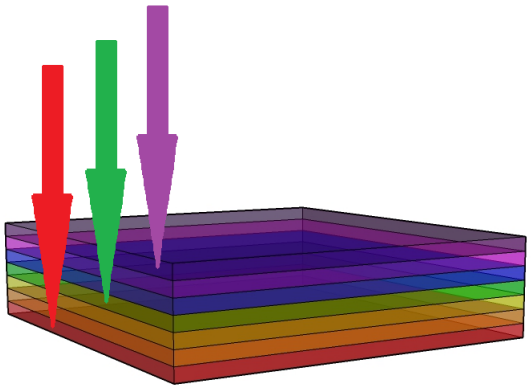

Figure 12: Cartoon depicting the notion of a vertically aligned free-carrier concentration gradient allowing for broad band absorption. Note how the long wavlength (red) penetrates the entire stack because the energy of the red photon is below the bandgap of the preceding layers.

for HMMs and thus a similar solution is likely to be a remedy.

In Fig. 22 the absorption characteristics of a high quality surface plasmon mode are depicted. Essentially, at frequencies where the (metallic/conductive) material of interest has a low loss and a large magnitude of the real part, we can find an angle of incidence for a given frequency which results in nearly perfect absorption as well as the formation of surface plasmon modes. To overcome the combined issues of angular acceptance and low-loss regions with limited bandwidth, we note that multi-layer HMMs whose metallic constituents are arranged to give a gradient in carrier concentration decrease the angular selectivity and increase the availability of the various low loss regions that correspond to the appropriate plasma frequencies in the material. This platform will likely see some form of realization as it is one of the few currently available mechanisms to achieve broad band low loss plasmonics without the use of a grating structure.

CHAPTER 3: REVIEW OF PUBLISHED DATA

3.1 Epitaxial HMM Fabrication and Characterization

Recent progress in the area of HMMs has sparked interest in transparent conductive oxides (TCOs) that behave as plasmonic media in the near-IR and optical frequency range for imaging and sensing applications. It has been shown that by depositing alternating layers of negative-epsilon/positive-epsilon materials, a medium can be created whose index can be tailored to be near zero. Modeling structures with sub-unity-magnitude indices of refraction reveals properties that enable evanescent fields containing sub-wavelength information to be coupled to propagating radiation. We investigate the optical, electronic, and physical properties of radio frequency plasma-assisted molecular beam epitaxial (RF-MBE) growth of alternating layers of ZnO and TCO of uniform thickness for HMM applications. Preliminary work creating ZnO and Al-doped ZnO (AZO) has shown a negative real part of the permittivity at near-IR whose modulus is proportional to the number density of Al dopant. However, increasing the Al content of the AZO increases the transmission losses to unacceptable levels for device applications at industry standard telecommunication wavelengths e.g. 1.33 μm and 1.55 μm. A TCO with conductivity and physical structure superior to that of AZO is gallium-doped ZnO (GZO). Properly grown GZO has been demonstrated to possess improved crystal quality over AZO due to the higher diffusivity of Al in the ZnO.

At the time this work began (mid 2012), ZnO had begun to receive significant attention from the HMM and plasmonics communities as a semiconductor material of interest. It may also be a result of coincidence, as many of the well-recognized names in semiconductor HMMs are also familiar to anyone working in the field of transparent conducting oxides. We began by using the MBE facilities at UNC Charlotte to try and evaporate zinc in an oxygen plasma ambient to grow ZnO on sapphire (α-Al_2O_3). The use of an effusion cell proved to be somewhat problematic for our reactor's configuration and so an experiment was attempted where the MBE's electron beam evaporator was loaded with a crucible full of 7N (99.99999%) pure zinc. This technique delivered much better results than the use of the effusion cell and eventually reasonable quality thin films were obtained. The doping of the zinc was accomplished by evaporation of gallium from an effusion cell. To create the doping gradient, the gallium cell is tuned on and off as the electron beam crystal thickness oscillator counts the approximate deposition rate. Further details of the growth procedure are detailed elsewhere [20].

After growth the samples were subjected to a full array of characterization techniques including Hall effect, XRD, FTIR spectroscopy, IR and VIS ellipsometry, and SEM w/EDAX (Energy Dispersive Analysis X-ray). The conductivity data combined with information from the spectral characteristics of the ZnO/GZO thin films allows us to infer a reasonable amount of information about the doping mechanisms and plasma frequency of the material.

The process of characterizing the IR properties of our HMM begins with having a complete knowledge of the optical properties of our c-plane sapphire substrate. The properties of sapphire being relatively well known in the literature, values for n and k were easy to

obtain by fitting the ellipsometry data. Shown below in Fig 13 is the plot of the obtained values.

With the optical substrate properties in hand, we can then turn our attention to attempting

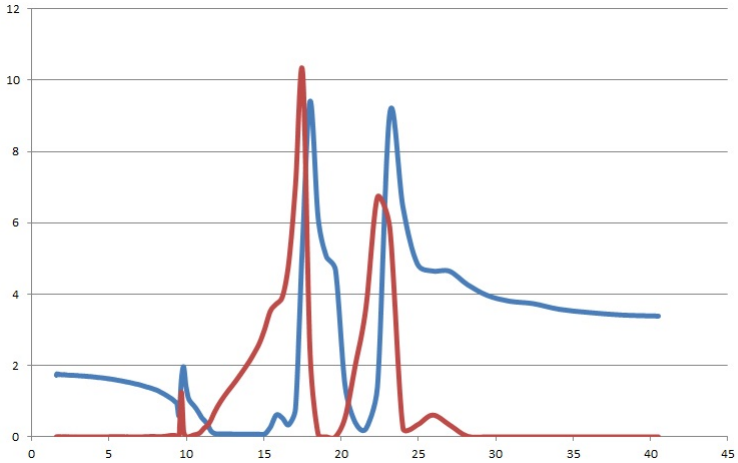

Figure 13: Ellipsometry of bare c-plane sapphire showing the index of refraction (blue) and extinction coefficient (red) from 2 to 40 μm

to characterize the HMM. Though determined in hindsight, the proper method for characterizing a HMM by variable angle spectroscopic ellipsometry (VASE) would follow the following procedure:

1. Identify the candidate materials to be used as multi-layers components and substrate
2. Characterize the substrate using VASE
3. Measure the surface RMS roughness of the substrate by AFM
4. Measure the substrate diffraction peak by XRD
5. Deposit a thin film of each of the candidate materials on the same type of substrate

6. Measure the surface RMS roughness of each film my AFM
7. Measure the strain/relaxation of the films by XRD
8. Characterize the individual films by VASE
9. Deposit one of the materials on the other and characterize by VASE
10. Measure the surface RMS roughness of the bi-layer by AFM
11. Measure the stress/strain of the bi-layer by XRD
12. Proceed to develop a multi-layer HMM by repeating this process until the contribution of each step to the end result is well understood

With the data available from the bare substrate we then characterize a 16-layer HMM made of ZnO and GZO on c-plane sapphire by VASE. To fit the HMM on a substrate, an attempt was made using the WVASE software to subtract the substrate from the HMM. This is in fact a very challenging task in the mid-to-far-IR spectrum due to complex scattering and interactions with optical phonons. Past 20 μm the results shown in Fig 14 below may not be accurate as the FTIR resolution decreases with increasing wavelength.

In order to ascertain a reasonable estimate of the accuracy of our VASE results, we turn to a Perkin-Elmer FTIR. Though only available at normal incidence, the FTIR can let us known whether or not there are significant errors in our data. It is also advantageous in that it gives an immediate result which requires no interpretation.

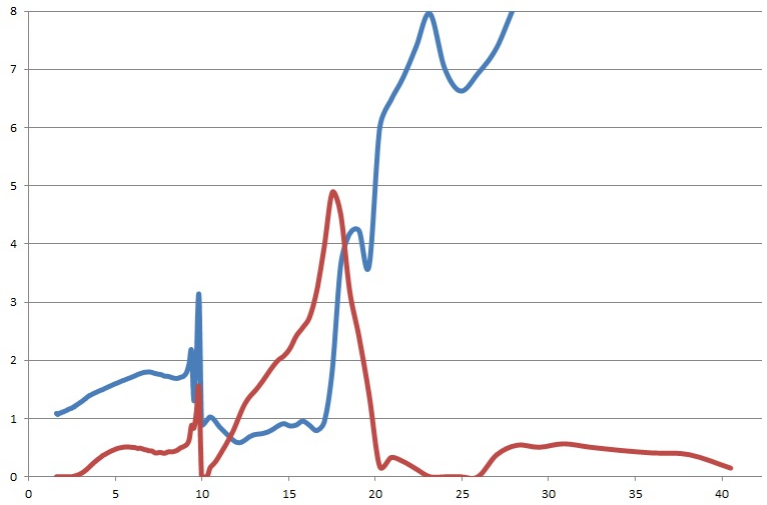

Figure 14: Ellipsometry of 16-layer ZnO/GZO HMM showing the index of refraction (blue) and extinction coefficient (red) from 2 to 40 μm

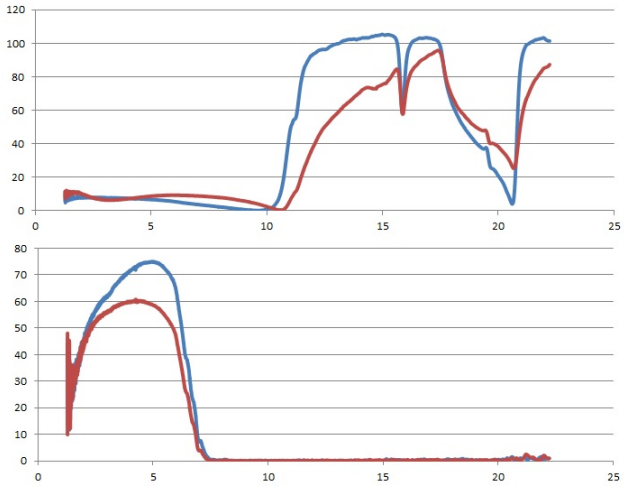

Figure 15: FTIR of 16-layer ZnO/GZO HMM (red) and bare sapphire (blue) substrate showing reflection (top) and transmission (bottom) from 2 to 22 μm. Y-axis is measured signal intensity relative to a gold mirror reference, x-axis is wavelength in μm.

Looking at Fig 16 we can see that both results are in good agreement. There are noticable differences between the FTIR and VASE results, but they are direct consequences of the difference between the resolution of the two systems and angle of incidence. It is important to note that the reflection and transmission values from the ellipsometer are actually derived

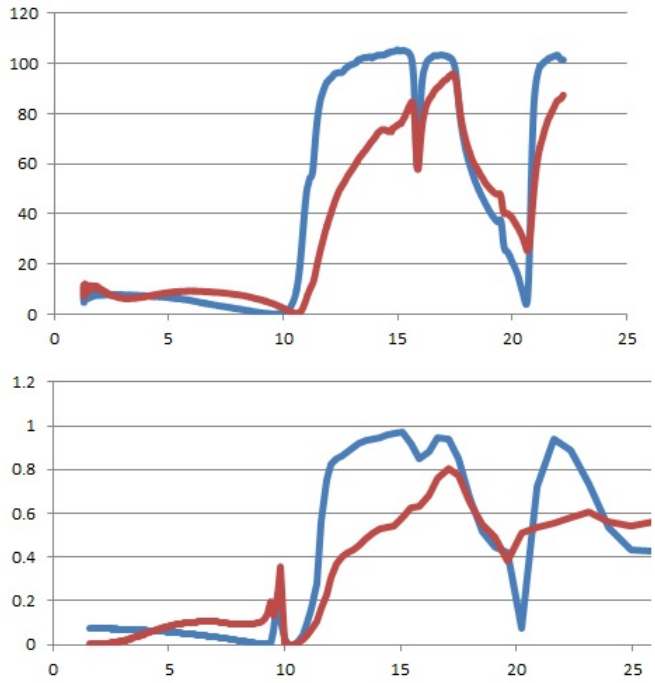

Figure 16: FTIR of 16-layer ZnO/GZO HMM and bare sapphire substrate (top) compared to VASE scan (bottom) of 16-layer HMM and sapphire substrate from 2 to 25 μm. Y-axis is measured signal intensity relative to a gold mirror reference for the top graph and calculated reflectance from VASE analysis on the lower graph, x-axis is wavelength in μm

from the extracted n and k values using the method detailed in [17] whereas the FTIR directly measures transmission and reflection. It is thought that the spike in the VASE plot near 10 μm can be attributed to unincorporated metal particles which exist in both the HMM and the sapphire substrate. As such, we're confident that we have a good estimate of the IR optical properties of our HMM as fabricated.

Continuing the notion of push button characterization, Fig 17 shows a plot of the absorption determined by 1-T-R=A. While there are some discrepancies due to scattering, one can see that the measured absorption is in agreement with the preceding reflection and transmission data.

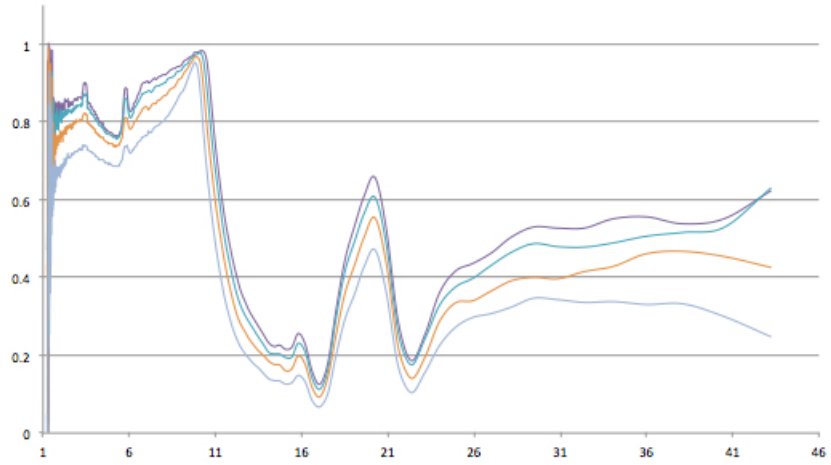

Figure 17: Showing plot of absorption vs wavelength from 2 to 40 μm determined by subtracting measurements of R and T for angles of incidence of 40-70 degrees

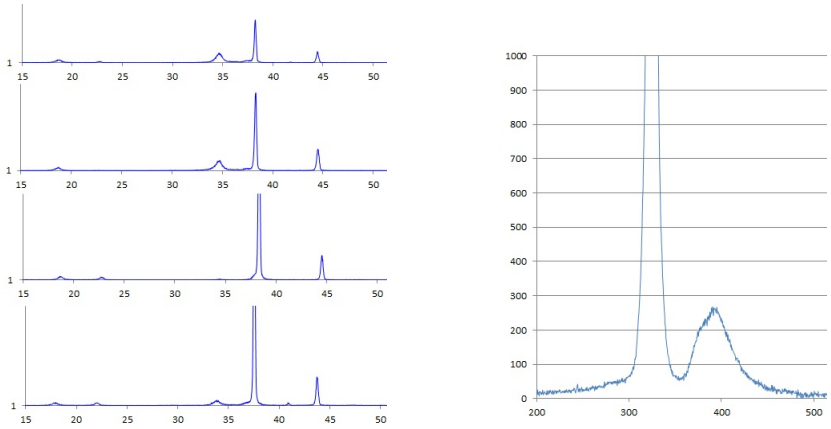

Figure 18: $2\theta - \omega$ XRD scans of HMM structures showing ZnO (002) peak at approximately 34.5 degrees (left) Photoluminescense of HMM excided by HeCd laser (right)

Fig 18 shows $2\theta - \omega$ plots from a Panalytical Xpert Diffractometer which reveal both strained and relaxed polycrystalline phases of ZnO/GZO. The strong peak at 38^o is from the substrate. It is instructive to consider the properties of the crystalline lattice of a semiconductor as strain can act as a doping mechanism, especially in ZnO [46]. Sometimes called strain-induced doping, this apparent change in the free carrier concentration causes us to adjust our estimates of the effect of doping on the material's electrical and optical

properties. Also in Fig 18 to the right of the XRD data is a photoluminescense plot of the HMM illuminated with a HeCd laser. The large spike at 320nm is the laser, the small bump at 400nm is the only photoluminescent carrier recombination observed. This is presumably due to an extremely small minority carrier concentration as well as low mobility and poor quantum efficiency typical of a polycrystalline film.

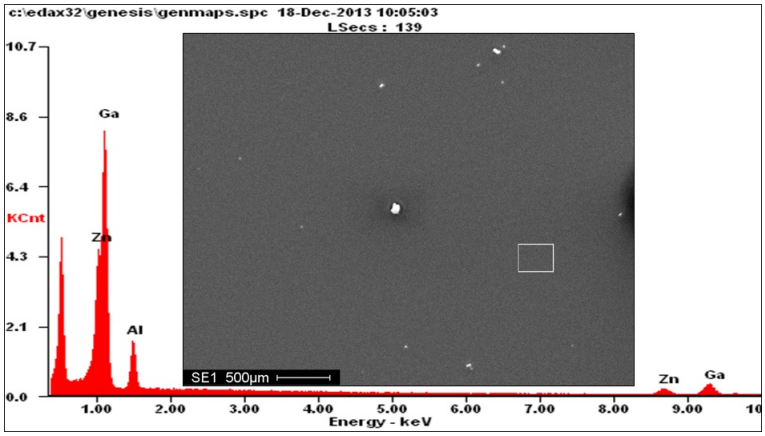

Figure 19: EDS plot with superimposed SEM image of HMM surface. Note the zinc particles which dot the surface. These inclusions are incompletely evaporated zinc from the electron beam.

In Fig 19 above, the EDS plot and SEM image are shown for the 16-layer ZnO/GZO HMM. The use of electron spectroscopy to determine stoichiometry proved to be problematic in multi-layer thin films. EDS is ideal in a scenario where a relatively thick film is on a bulk substrate with an entirely different composition. The case where we have multiple very thin films on a substrate which shares a common element with the film is the worst case scenario for this method.

The other aspect of our group's work with HMMs at UNC Charlotte consists of FEM simulations of HMMs with a similar configuration to those that we have fabricated. Our intent is to show good agreement between our experiments and our simulation work to

verify that we have a firm understanding of the physics and material properties at play. The simulation work began in Singapore as part of a NSF sponsored initiative to encourage international collaboration. We began by modeling 16-layer ZnO/GZO HMMs in CST Microwave Studio for the purpose of studying the transport of high-k modes in HMMs.

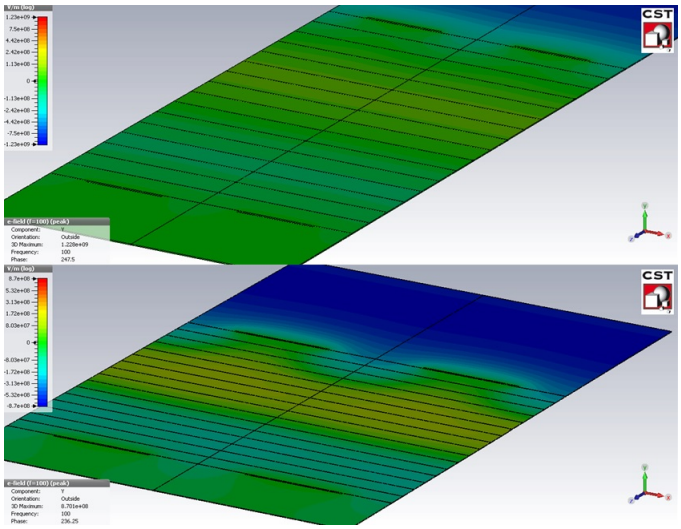

Figure 20: Two simulation results for the electric field in 16-layer ZnO/GZO HMMs for high and low loss regions of operation. Note the enhancement of the field in the lower picture indicating enhanced transmission of high-k modes

Once the CST simulations predicted reflection and transmission values that were approximately equal to those which were measured for the real-world HMM structure, the simulation parameters were then considered to be representative of the actual values. A keen eye will also notice the presence of a pair of thin black lines on the front and back surfaces of the HMM. In order to study the interaction of evanescent modes in a FEM solver which is using Maxwell's equations, one must first address the challenge of creating those evanescent modes. One method of creating evanescent fields is to drive a waveguide below its cutoff frequency. However, the complexity added to the problem by convolving the waveguide's modal response with that of our material under test makes this method

undesirable. Our desired solution, then, is to create evanescent field in the HMM by using a subwavelength grating. Subwavelength gratings act like normal diffraction gratings with the exception that all but their 0^{th} order modes are evanescent. The normal equation which describes the effect of a diffraction grating on the wave vector is

$$k = k_o \pm \frac{2\pi n}{\Lambda} \tag{29}$$

where k is the free space wave vector at the interface, n is a positive integer, and Λ is the spatial period of the grating. It is critical to keep in mind that the simultaneous addition and subtraction of this momentum is conducive to momentum conservation. However, the grating adds virtual momentum which causes the relationship between the wave vector in free space and the wave vector in the HMM to differ. This fact is key to our desired result: a method for determining and subsequently engineering the evanescent mode interaction in HMM. Since the spatial period defines the transverse momentum, we can vary the spatial period to obtain the dispersion for evanescent waves in HMMs for our specific material combination. The final result is Fig 21 below.

By running nested parameter sweeps in CST which iterate through frequency as well as the spatial period of the grating seen in Fig 20, we assemble the data set required to produce the above image. The data was compiled as a 2D array of scalar data in MATLAB and then plotted as shown. The bright yellow band which intercepts the x-axis at approximately $\frac{k_x}{k_o} = 1.25$, represents the usable transmission window for this HMM in which evanescent modes can be transferred effectively.

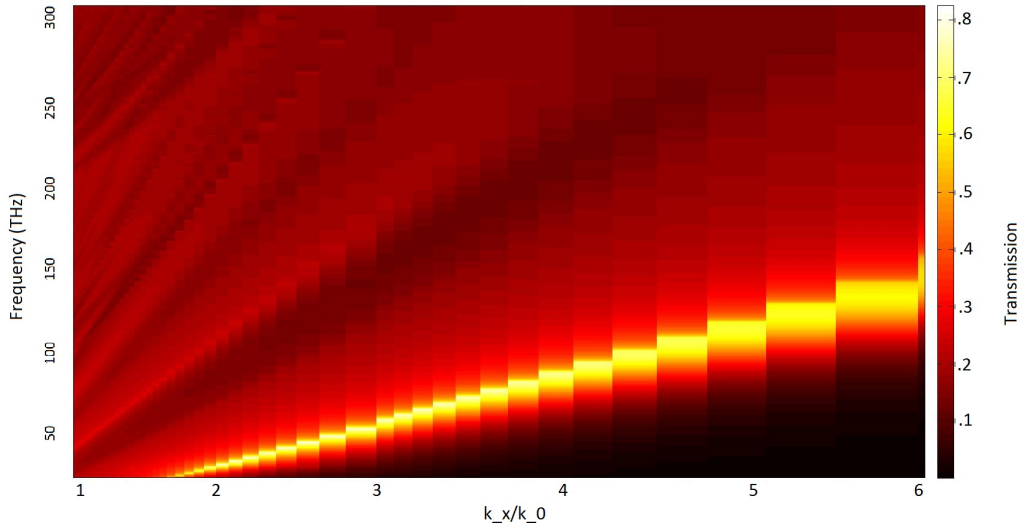

Figure 21: Normalized transmission plot for 16-layer ZnO/GZO HMM from 30-300 THz (y-axis) as a function of the normalized transverse momentum parameter $\frac{k_x}{k_o}$ (x-axis).

Recently the potential for using surface plasmon resonance for sensing and sub-wavelength optical communication has emerged as one of the most popular topics in material science and optics. Surface plasmons offer an unrivaled advantage in their ability to maintain the information encoded in the wave functions of propagating EM waves as electron oscillations that have a spatial period which is shorter than the free space wavelength of the EM wave they are driven by. This is a classic example of a polariton, which is a strongly coupled light-matter interaction. As a result, surface plasmon polaritons provide one of the only systematic mechanisms with which the diffraction limit of light can be overcome. Since plasmonic devices can be used for a wide range of applications it was natural to investigate whether or not HMMs are useful as plasmonic media.

Using COMSOL's RF Module, the same dispersion relations from the aforementioned CST simulations were used for the sake of making comparisons between CST and COMSOL. At the same time an effort was begun to see if surface plasmon resonance was a

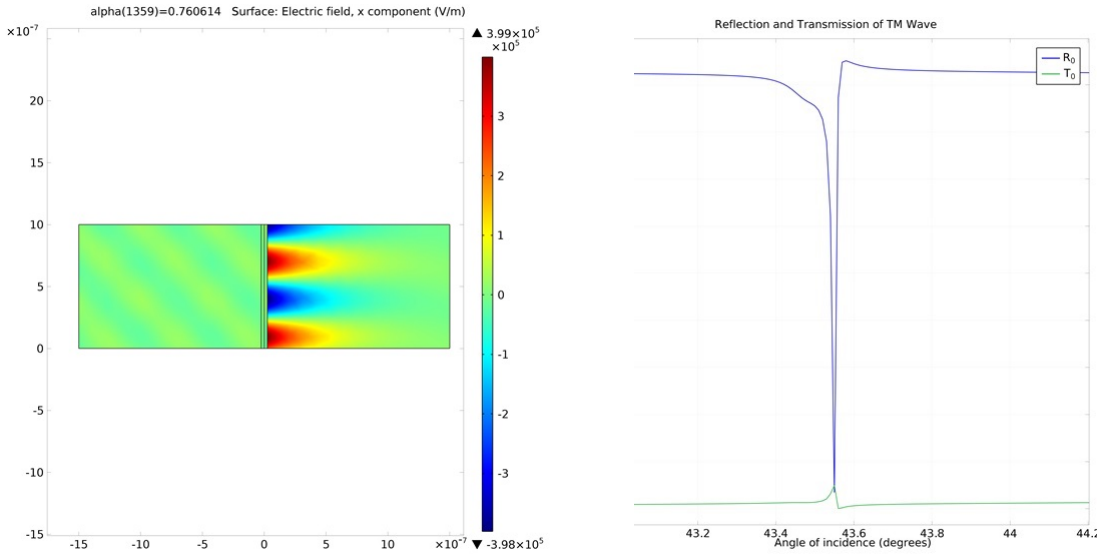

Figure 22: Showing a plot of the electric field enhancement due to the formation of a surface plasmon resonance (left). Note the incident field to the left is almost invisible due to the dynamic scaling of the E-field range. On the right is a reflection (blue) and transmission (green) plot for the surface plasmon resonance shown on the left. Note the very sharp and narrow dip in the reflection and the nearly perfect absorption which correspond to the angle at which the surface plasmon resonance is a solution to Maxwell's equations

phenomena that COMSOL could predict. Before continuing, we offer a brief summary of the representations used herein for dealing with plasmon polaritons. Beginning with Eqn 30, which is derived in detail in [17] we can draw on some simple mathematical observations to gain physical insight into the material properties which give rise to surface plasmon polaritons. This is the equation for a simple metal-dielectric interface and gives some insight as to why it is important to keep coupling efficiency in mind when considering surface plasmon polaritons.

$$k_{SP} = k_o \sqrt{\frac{\varepsilon_D \varepsilon_M}{\varepsilon_D + \varepsilon_M}} \tag{30}$$

We initially know that the wave vector which describes an evanescent field is characterized by its imaginary part. Therefore, we expect the net result under the radicand to be negative. In principal this occurs when the magnitude of ε_D is greater than the magnitude

of ε_M. Without any grating or other coupling structure surface plasmons only exist when dispersion relations of the metal and dielectric provide a bandwidth over which $|\varepsilon_M| < |\varepsilon_D|$ and $\varepsilon_M \cdot \varepsilon_D < 0$. The dependence of surface plasmon polaritons on the loss term of the permittivity at flat metal-dielectric interfaces is all confirmed by COMSOL as lossless materials will not reveal the field enhancement characteristic of surface plasmon resonance shown in 22 as well as in [82]. These results are also noteworthy because they show that a simple flat dielectric surface with a non-unity index can be used to couple to surface plasmon modes at a narrow range of angles. This allows one to utilize the latest nano manufacturing techniques to tune polymers by doping and photo polymerization to realize gradient index dielectric nanostructures to couple into plasmon modes for sub-wavelength free space to plasmonic couplers.

In a FEM solver, surface plasmons appear as periodic sinusoidal variations in the electric field intensity at a flat interface. They are strong enough to cause the incident radiation that formed the plasmons to be almost invsible due to dynamic range issues in the displayer scaling as shown above in Fig 22. The attempt at obtaining strong surface plasmon response in the 16-layer ZnO/GZO HMM did not yield an encouraging result in COMSOL. The evanescent field enhancement favors a low index material on the back side of the interface to maximize the momentum discrepancy giving rise to the surface plasmon condition. This adds another degree of complexity to designing HMMs for multi-layer plasmonics. In the future, mitigating loss mechanisms and remembering the existence of surface plasmon resonance will serve anyone working with HMMs well. The conclusion drawn is that at present the loss in our structure is undesirably high in the region where our HMM has its

type-II characteristics. This naturally leads to the discussion of HMM electrodynamics and usable HMM bandwidth.

Having identified the necessary condition to obtain a hyperbolic dispersion profile, one is still left with the contents of the periodic table as the limiting design space for the choice of HMM materials. To begin to understand the properties of ZnO and GZO in the infrared a literature search was initiated to look for phonon resonance frequencies and damping rates. In the mid-to-far infrared range, the coupling of photons to phonons becomes the dominant absorption mechanism [45]. Furthermore, the responses of optical phonons in crystalline thin film materials are known to be isotropic and different from the bulk value [8]. Using the data available from [10, 45, 8] Fig 23 shows the dispersion relations for the normal and transverse components of the permittivity that were obtained by iteratively adjusting the damping rates and resonance frequencies until the simulated reflection and transmission spectra were in good agreement with the experimental data.

It is worthwhile to note that the phonon resonance frequencies can have a significant effect even microns away from the absorption peak. This is a result of the FWHM of the phonon resonance, which is a function of the microstructure of the film in this case. With the dispersion relations in hand which accurately represent our 16-layer ZnO/GZO HMM on sapphire, we can then check to see in which frequency ranges our material behaves as a HMM.

The HMM mode of operation was determined with a simple routine in MATLAB which checked the signs of $\varepsilon_{\perp}$ and $\varepsilon_{||}$ as a function of frequency. The ranges over which $\varepsilon_{||}$ is

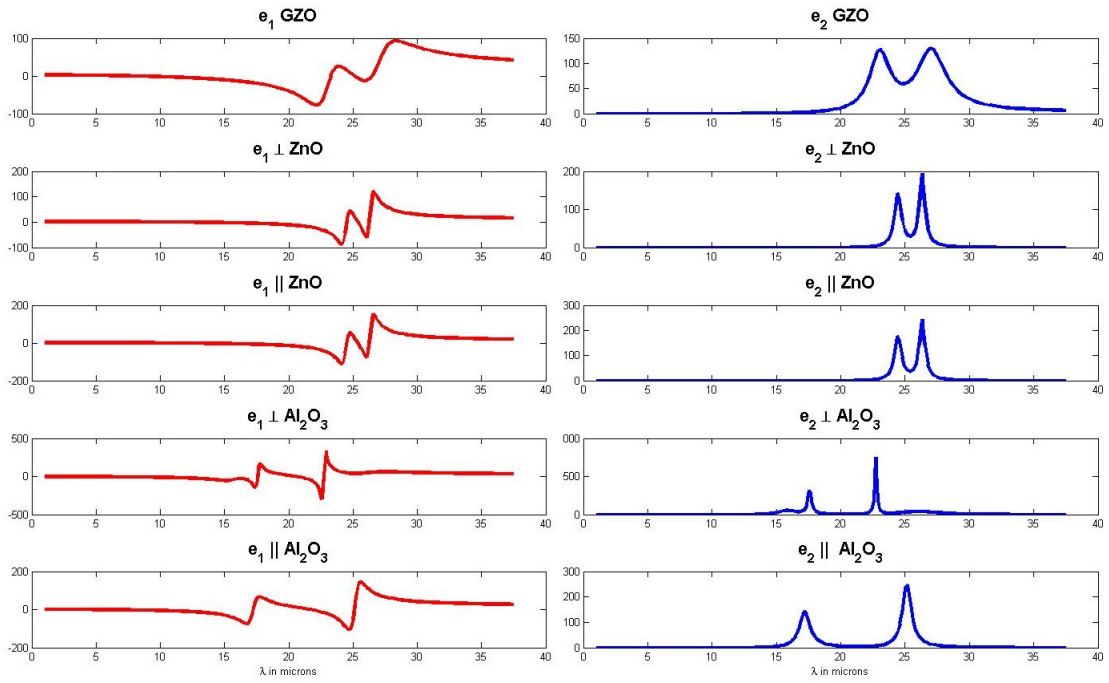

Figure 23: Showing real and imaginary components used to form the permittivity tensors for the 16-layer ZnO/GZO HMM. X-axis is wavelength in μm. Y-axis is in units of Farads/meter. e_1 and e_2 denote the real and imaginary parts of the dielectric function, respectively.

Material Mode	Range (μm)
normal	2.0 - 9.09
type I	9.09 - 10.56
normal	10.60 - 10.83
type II	10.87 - 13.39
normal	13.43 - 24.35
type II	24.39

negative and $\varepsilon_\perp$ is positive are labeled as type I HMM while the opposite correspond to a type II in accordance with the conventions previously used within this document and the open literature. To the uninitiated working in mid-to-far IR optics, the ranges over which the permittivity can vary can be somewhat shocking. In the visible a permittivity of 10 could be considered reasonably high. Near a sharp optical phonon absorption peak, the swing in the real part of the permittivity can be on the order of hundreds of F/m.

Due to the strongly polar nature of the chosen materials, the anisotropy in the infrared spectrum is rather strong. For the case of HMMs, this is desirable. Anisotropy is a critical requirement for indefinite media and stronger the anisotropy, the more dramatic the HMM properties.

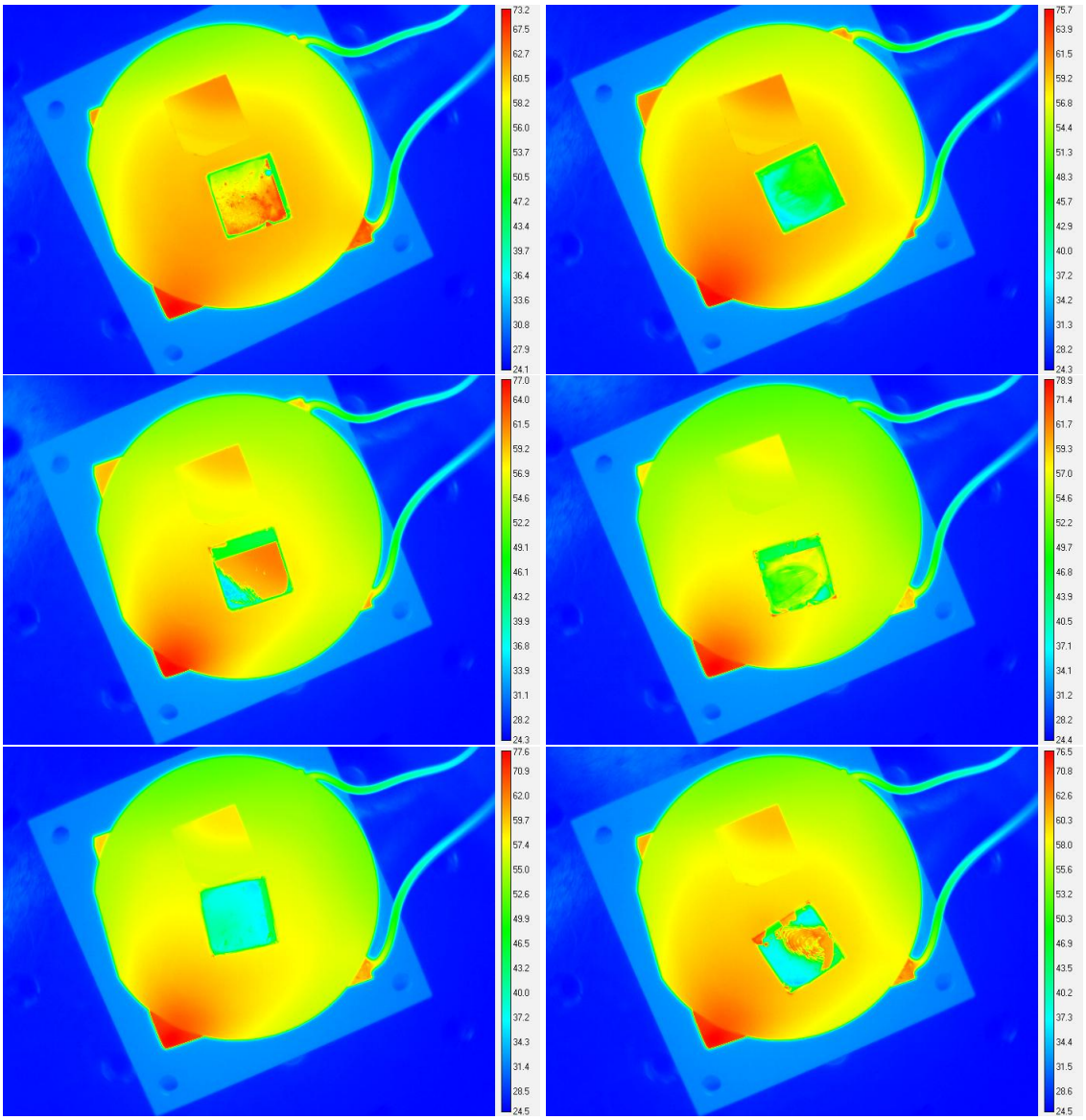

Figure 24: FLIR-IR Thermal images of gold diffraction gratings on 16-layer ZnO GZO HMM

The last step taken in this research at present was the fabrication of 50/50 duty cycle 2μm grating structures made of gold on top of our HMM structures in order to attempt to observe enhanced radiation through grating-coupled high-k modes. Fig 24 shows 6 IR images taken from a FLIR IR camera. The top sample is a control made from homogeneous GZO while the bottom sample is a 16-layer ZnO GZO HMM with a 2μm grating. In the background

one can see the heat sink onto which the Peltier heater is mounted. The samples sit on a sapphire wafer identical to the one on which the samples are prepared. This serves as an additional experimental control. In the top left picture one can see that there are parts of the HMM sample which appear to the camera to be as hot as the Peltier heater which acts as the thermal source. This is an interesting result which indicates that future work should focus on studying the underlying physics behind the grating to HMM coupling interactions which are most likely responsible for the effect.

3.2 HMM Colimators

Having fabricated and characterized GZO/ZnO HMMs, the next logical step was to develop a device which demonstrated the unique, intrinsic properties of HMMs. As previously mentioned, a type II HMM will act as a perfect metal along the direction matching the surface normal. In contrast, the type II HMM acts as a lossy dielectric in the plane of the film. This is readily apparent from examining the projection from a bounded k-space isofrequency contour to the HMM hyperboloid. To provide a predictive illustration of the bulk electromagnetic directivity of type II HMMs, a simple COMSOL simulation was executed in order show the effects of the generalized reflection coefficient equations at a boundary where the index of our material is less than unity.

$$r_{\mathrm{TE}} = \frac{\eta_2 \sec(\theta_2) - \eta_1 \sec(\theta_1)}{\eta_2 \sec(\theta_2) + \eta_1 \sec(\theta_1)} \tag{31}$$

$$r_{\mathrm{TM}} = \frac{\eta_2 \cos(\theta_2) - \eta_1 \cos(\theta_1)}{\eta_2 \cos(\theta_2) + \eta_1 \cos(\theta_1)} \tag{32}$$

Equations (31) and (32) show the generalized reflection coefficients where loss may be considered. Sometimes mistakenly identified as Fresnel's equations, it should be noted

that these coefficients are in terms of complex impedance ($\eta = \sqrt{\frac{\mu}{\varepsilon}}$) rather than index, and are implicitly more physically meaningful when dealing with boundaries. While the two may seem interchangeable under the proper transformations, it can be shown that index of refraction only relates to the steady state phase compression of an electromagnetic wave in a material. To be clear, this means that index of refraction is of questionable use for the evaluation of transient phenomena if there is any appreciable absorption in the system of interest. Transient electrodynamic phenomena are best modeled using impedance boundary conditions.

3.3 Direct Laser Writing

Direct laser writing via two photon polymerization has enabled previously unavailable degrees of freedom in the additive fabrication of micro-to-meso scale structures. The structures produced by these techniques are ideally suited to create optical devices which operate from the THz regime to the near infrared spectrum into the visible spectral range. Here we report on the infrared dielectric response of two monomers IP-Dip and IP-L after polymerization which are frequently employed in commercial two photon lithography tools from Nanoscribe over the spectral range of 250 cm^{-1} to 6000 cm^{-1}. A parameterized dielectric function model is presented and discussed.

The advent of commercially available nanoscale 3D direct laser writing (3D-DLW) systems has led to a rapid expansion of the application space available to researchers employing additive manufacturing techniques for the fabrication of 2D and 3D structures with features ranging from the nanometer to millimeter scale. Initially, the fields of structural and acoustic mechanics were the central focus of publications reporting on the properties

of materials produced by 3D-DLW processes. A representative example of this initial effort is the work by Bückmann *et al.* where it has been shown that 3D-DLW of polymer structures can lead to materials which can cloak mechanical motion [6]. Recently it has been demonstrated that two photon polymerization can provide base elements from which materials exhibiting mechanical strengths that approach the theoretical maximum of the constituent materials can be created [3].

Interestingly, the characteristic feature scales that make the 3D-DLW processes attractive for mechanics and acoustics also lend themselves to the design of long wavelength optical components such as printable optoelectronics, THz imaging and sensors, infrared optical devices, etc. This relatively new application of additive manufacturing processes for the fabrication of designed optical materials may have significant impact as early works have already demonstrated that printable optical interconnects exhibit performance that is suitable for industrial telecommunications applications [41, 60]. More recent works have shown very encouraging results on materials and devices for the mid-infrared spectral range for instance broadband dichroic circular polarizers and photonic crystals with measurable band gaps [30, 55].

In addition to the advancement of optical components in the infrared spectral range, it has been demonstrated that with care, two photon lithography can be extended toward the realization of components intended to work in the visible spectrum. One example is the use of structures fabricated by 3D-DLW in order to realize a plasmonic control of liquid crystals [18].

Although there is a rapidly growing effort to apply 3D-DLW techniques to fabricate materials for THz and infrared applications, accurate infrared dielectric function data on the some of the most commonly used monomers have not yet been reported. This hinders both the understanding of the scattered fields from structures designed to operate in the infrared in measurement and simulation as well as the simulation-based design of materials with novel properties.

In this dissertation we report on the first mid-infrared ellipsometry experiments to determine the complex dielectric function of two polymerized monomers which are frequently used in the Nanoscribe 3D-DLW process named IP-Dip and IP-L [48]. These monomers have different viscosities, indices of refraction, and intended uses. IP-Dip is recommended for use in standard and inverted 3D-DLW configuration. IP-L can be used in an inverted oil immersion configuration wherein the laser beam writes through a transparent substrate into the IP-L. A parameterized model dielectric function is derived and discussed.

The samples investigated here were prepared by means of spin coating IP-DIP and IP-L at 5000 rpm for 4 minutes. Highly-doped ($\rho \simeq 0.003$ Ω·cm), 4 inch $< 100 >$ silicon wafers were used as substrates according to the best practices detailed in [68]. Prior to the spin coating the substrates were carefully cleaned by immersion in CMOS grade acetone for 5 minutes followed by a DI rinse and 5 minutes of immersion in CMOS grade methanol. Afterward, each substrate was dried manually with nitrogen, cleaned in a 3:2 mixture of 96% sulfuric acid and 30% hydrogen peroxide for 20 minutes, and then thoroughly rinsed in DI water. After the spin coating the adhered monomers were polymerized in a UV oven over the course of 30 minutes. The sample preparation was carried out in a class 100 clean

room to ensure purity of the films.

The cured IP-Dip and IP-L polymer film samples were measured on a commercial infrared ellipsometer (Mark I IR-VASE®, J.A. Woollam Company). The instrument is equipped with a Boman FTIR source and a DTGS detector and operates in a classical rotating polarizer - sample - rotating compensator - rotating analyzer configuration as is detailed in [19]. Ellipsometric Ψ and Δ data were acquired over the spectral range from 250 to 6000 cm^{-1} with a resolution of 2 cm^{-1} at three angles of incidence: $\Phi_a = 60^\circ$, 65°, and 70°. The quantities of interest, Ψ and Δ, represent the ratio of reflected transverse magnetic to transverse electric polarizations and the relative optical path difference, respectively. The measurements were carried out under normal ambient conditions while the room temperature was kept at approximately 21°C.

The optical modeling and data analysis was carried out using a commercial ellipsometry data analysis software package (WVASE32™, J.A. Woollam Company). The complete ellipsometric data set obtained for each sample was fit to a stratified layer optical model. The optical model consists of ambient/polymer thin film/Si substrate. Separate parameterized dielectric function models were employed to describe the infrared optical response of IP-DIP, IP-L, and the doped Si substrate.

The infrared dielectric functions of both IP-Dip and IP-L are described here using a mixed oscillator model which was first introduced by Synowicki and Tiwald [67]. Synowicki and Tiwald demonstrated that combinations of oscillators with Gaussian and Lorentzian broadening can be combined with Tauc-Lorentz oscillators in order to describe the dielectric response of different materials over a wide spectral range from the infrared to the

vacuum ultraviolet [67] using functions with physically relevant parameters. The advantage of phenomenological mixed oscillator models is that typically a reduced number of parameters is required in order to accurately describe the experimentally observed optical response. Here we employ a combination of oscillators with Gaussian and Lorentzian broadening to describe the infrared dielectric function of IP-Dip and IP-L monomers after polymerization:

$$\begin{aligned} \varepsilon &= \varepsilon_1 + i\varepsilon_2 = \\ &\varepsilon_\infty + \sum_i \mathrm{Lor}(A,\Gamma,\omega_0) + \sum_i \mathrm{Gau}(A,\Gamma,\omega_0), \end{aligned} \tag{33}$$

where the functions $\mathrm{Lor}(A,\Gamma,\omega_0)$ and $\mathrm{Gau}(A,\Gamma,\omega_0)$ indicate oscillators with Lorentzian and Gaussian broadening, respectively. The oscillator amplitude, broadening, and resonance energy are indicated by A, Γ, and ω_0, respectively. It will be demonstrated in the following section that IP-Dip requires a combination of 27 Gaussian and Lorentzian oscillators while IP-L required only 15 of the same two oscillator types.

Equations (34) and (35) show the Lorentzian and Gaussian forms for the imaginary part $\varepsilon_2^{\mathrm{Lor}}(\omega)$ and $\varepsilon_2^{\mathrm{Gau}}(\omega)$ of the complex dielectric function $\varepsilon(\omega)$, respectively:

$$\varepsilon_2^{\mathrm{Lor}}(\omega) = \frac{A\,\Gamma^2\omega_0\,\omega}{(\omega_0^2-\omega^2)+\Gamma^2\omega^2}, \tag{34}$$

$$\varepsilon_2^{\mathrm{Gau}}(\omega) = \mathrm{A}e^{-(\omega-\omega_0/f\cdot\Gamma)} + \mathrm{Ae}^{-(\omega+\omega_0/f\cdot\Gamma)}, \tag{35}$$

where $1/f = 2\sqrt{\ln(2)}$. The corresponding values for $\varepsilon_1^{\mathrm{Lor}}$ and $\varepsilon_1^{\mathrm{Gau}}$ are obtained by Kramers-Kronig integration of Eqs. (34) and (35) during the Levenberg-Marquardt analysis of the calculated Ψ and Δ data relative to the experimental values.

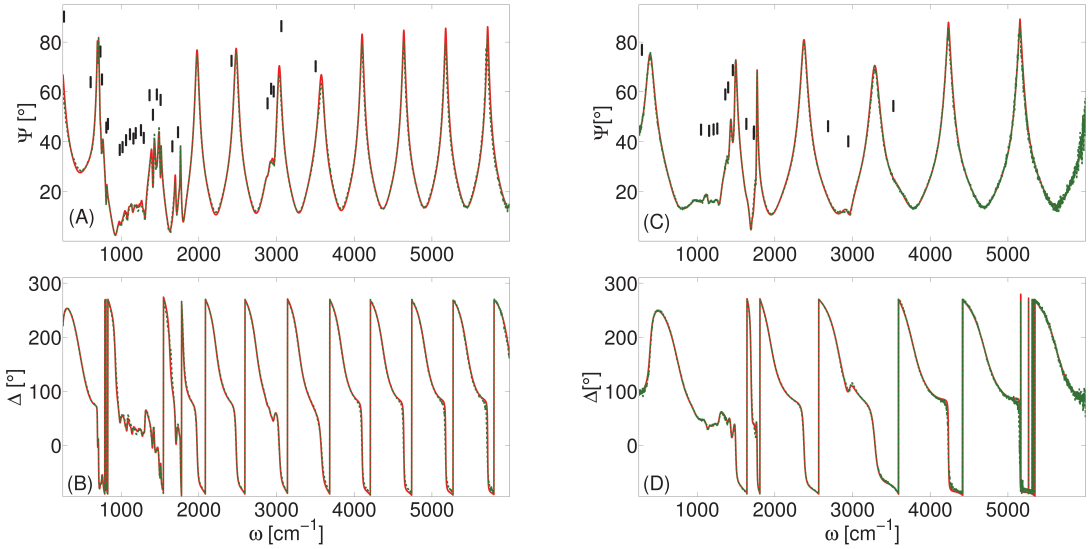

Figure 25: (A) and (C) Experimental (dashed green line) and best-model calculated Ψ data (solid red line) for the monomer IP-Dip (A) and IP-L (C) obtained at $\Phi_a = 65^\circ$. Vertical dash marks in (A) and (C) indicate the oscillator center energies listed in Tab. 1 and Tab. 2 below. (B) and (D) Experimental (dashed green line) and best-model calculated Δ data (solid red line) for IP-Dip (B) and IP-L (D) obtained at $\Phi_a = 65^\circ$.

The infrared dielectric function of the doped Si substrates is described using a classical Drude response where the resistivity ρ and the scattering time τ are accessible fit parameters. For the Si substrate which was used for the IP-Dip sample we obtained $\rho = (0.0031 \pm 0.0001)$ Ω·cm and $\tau = (13.7 \pm 0.2)$ fs. For the Si substrate which was used for the IP-L sample we obtained $\rho = (0.0032 \pm 0.0001)$ Ω·cm and $\tau = (13.1 \pm 0.1)$ fs.

Figure 25 depicts the experimental (dashed green lines) and best-model calculated (solid red lines) for Ψ (shown in (A) for IP-Dip and (C) for IP-L) as well as for Δ (shown in (B) and (D)) of polymerized IP-Dip and IP-L obtained at $\Phi_a = 65^\circ$. Note that while the data obtained at all three angles of incidence where analyzed simultaneously only the data for $\Phi_a = 65^\circ$ are shown here for clarity. An excellent agreement is found between the experimental and best-model calculated data, which are virtually indistinguishable in Fig. 25. Both IP-Dip and IP-L show a very similar infrared optical response where strong absorp-

Tab. 1 and Tab. 2 show the best-fit mixed oscillator parameters for the dielectric response of IP-Dip (left) and IP-L (right) from 250 to 6000 cm^{-1}. The oscillator energy ω_0, amplitude A, and broadening Γ are given in units of cm^{-1}. The letters 'G' and 'L' next to the oscillator number indicate whether the oscillator is Gaussian or Lorentzian. The best-fit value for ε_∞ is $\varepsilon_\infty = 2.37 \pm 0.01$ for IP-Dip and $\varepsilon_\infty = 2.22 \pm 0.01$ for IP-L. Error bars in parentheses [last digit(s)] represent the 90% confidence limits of the oscillator parameters shown above.

Table 1: IP-Dip best-fit oscillator parameters

i	ω_0	A	Γ
1 G	264 (13)	0.242 (6)	345 (26)
2 L	607 (5)	0.066 (4)	174 (16)
3 G	701.00 (3)	0.056 (4)	8.9 (8)
4 G	732.7 (7)	0.028 (5)	9 (2)
5 L	753.4 (4)	0.144 (3)	28 (2)
6 L	809.4 (3)	0.16 (1)	8 (1)
7 L	830 (4)	0.038 (5)	52 (11)
8 L	981.9 (9)	0.15 (1)	22 (4)
9 L	1018 (12)	0.18 (1)	141 (17)
10 L	1063 (1)	0.46 (3)	21 (3)
11 G	1113 (2)	0.15 (4)	32 (6)
12 L	1158 (3)	0.5 (3)	38 (10)
13 G	1188 (11)	0.5 (1)	59 (18)
14 L	1255 (1)	0.63 (3)	39 (5)
15 G	1291 (1)	0.12 (2)	24 (3)
16 G	1365 (4)	0.08 (6)	99 (12)
17 L	1408.8 (4)	0.22 (1)	12 (1)
18 G	1459.2 (6)	0.136 (4)	44 (1)
19 L	1507.7 (2)	0.11 (3)	7.9 (4)
20 L	1659 (1)	0.0586 (9)	169 (5)
21 G	1731.7 (1)	0.876 (4)	35.2 (2)
22 L	2420 (35)	0.0087 (1)	2495 (127)
23 L	2884 (2)	0.021 (2)	48 (6)
24 L	2930 (2)	0.025 (4)	51 (12)
25 G	2963 (1)	0.041 (5)	40 (3)
26 L	3062 (14)	0.0046 (4)	190 (31)
27 L	3503 (3)	0.0198 (4)	201 (6)

Table 2: IP-L best-fit oscillator parameters

i	ω_0	A	Γ
1 G	289 (8)	0.279 (4)	552 (10)
2 L	1050 (1)	0.342 (4)	143 (3)
3 L	1154.3 (8)	0.35 (2)	43 (3)
4 L	1211 (2)	0.64 (4)	77 (6)
5 L	1259 (3)	0.27 (5)	54 (7)
6 G	1362 (6)	0.089 (6)	105 (7)
7 L	1399 (1)	0.08 (1)	35 (7)
8 G	1459.6 (3)	0.142 (2)	36.0 (5)
9 L	1633.4 (6)	0.0474 (8)	64 (2)
10 G	1729.80 (9)	0.89 (2)	35.1 (2)
11 L	1731.9 (4)	0.21 (2)	58 (3)
12 L	2685 (11)	0.01214 (9)	1781 (34)
13 L	2945.3 (3)	0.07153 (4)	89.8 (9)
14 G	3336 (11)	0.0203 (8)	289 (14)
15 G	3525 (2)	0.039 (2)	197 (4)

tion bands are found in the range from 500 to 2000 cm^{-1}. The oscillator center energies are indicated as vertical dashes in Fig. 25. All best-fit model parameters including the confidence limits are give in Tab. 1 and Tab. 2 for IP-Dip and IP-L, respectively. The range from $\omega = 2000$ to 6000 cm^{-1} is transparent for both polymerized monomers as can be easily observed by the Fabry-Perot oscillations generated in the transparent films. Note that the frequency of these oscillations is significantly higher for the IP-Dip. IP-Dip has a

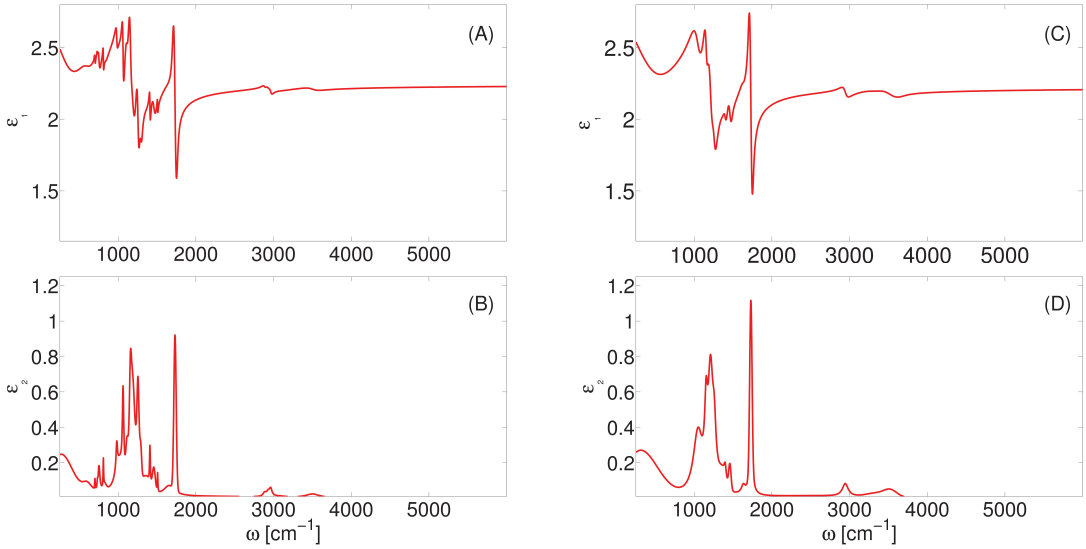

Figure 26: Best-model calculated real ($\varepsilon_1(\omega)$) and imaginary ($\varepsilon_2(\omega)$) part of the complex dielectric function $\varepsilon(\omega)$ for IP-Dip are shown in panels (A) and (B), respectively. Similarly, (C) and (D) depict $\varepsilon_1(\omega)$ and $\varepsilon_2(\omega)$ for IP-L. The major contributions to the dispersive behavior of both IP-Dip and IP-L occur between 1000 and 2000 cm^{-1}. The best-model parameters are given in Tab. 1 and Tab. 2.

higher viscosity compared to IP-L. This results in a significantly larger film thickness for IP-Dip $d_{\text{IP-Dip}}$ =7.474±0.002 μm while the thickness for IP-L is $d_{\text{IP-L}}$ =4.448±.001 μm when fabricated at the same spin speed during the deposition process described above. A few very weak absorption features can be identified in both polymerized monomers at approximately 3000 cm^{-1} and 3500 cm^{-1}.

The real and imaginary parts of the best-fit model complex dielectric function are depicted in Fig. 26 for both IP-Dip and IP-L. The infrared dielectric response of both polymerized monomers is dominated by two strong absorption lines around 1200 and 1600 cm^{-1}. However, comparing Fig. 26(B) and Fig. 26(D) it is readily apparent that while IP-L shows a relatively simple structure, IP-Dip shows a large number of narrow resonances. In fact, the dielectric function for IP-Dip gives evidence of a more complex chemistry as it takes nearly twice as many oscillators to fit IP-Dip compared to IP-L such that a good match

between the experimental and best-model calculated data is obtained as shown in Fig. 25.

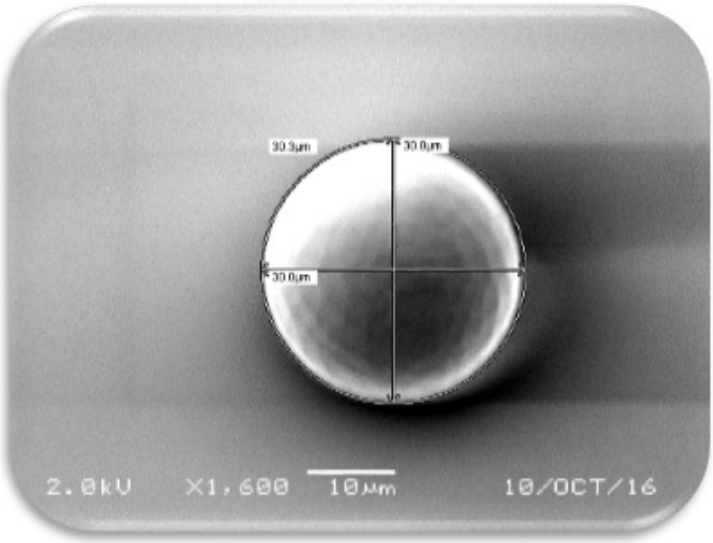

Figure 27: Microsphere produced by 3D-DLW in a Nanoscribe Photonic Professional GT system. This structure was produced as part of a study of the intrinsic form birefringence in 3D-DLW structures and is currently being used to generate forthcomming publications.

We have determined the complex dielectric function of polymerized IP-Dip and IP-L, two monomers which are frequently used in two photon polymerization with commercial direct laser writing tools. A mixed oscillator model composed of oscillators with Gaussian and Lorentzian broadening was found to appropriately render the dielectric response. Comparing the dielectric functions of IP-Dip and IP-L shows that IP-Dip exhibits almost twice as many discrete resonances which is interpreted here as an indication a more complex chemistry. We anticipate that the parameterized dielectric function reported here will help to improve first-principle calculations of the infrared optical response of 2D and 3D structures composed of these materials.

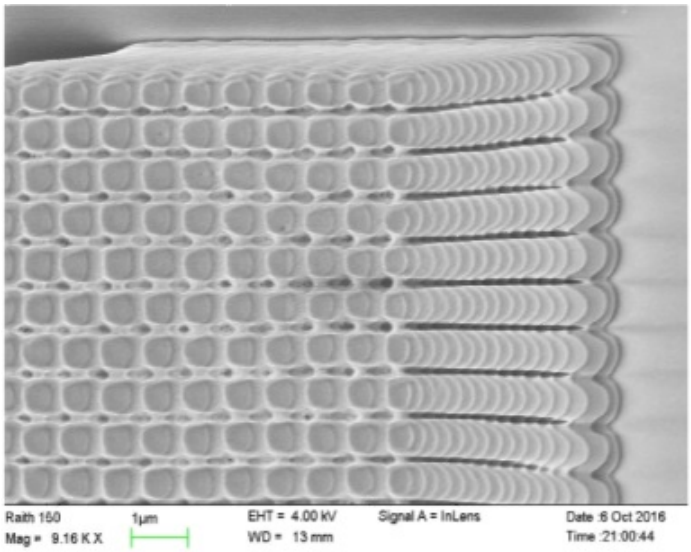

Figure 28: Nanowire array produced by 3D-DLW in a Nanoscribe Photonic Professional GT system. Note the tilt of the wires. This structure was produced as part of a study of the intrinsic form birefringence in 3D-DLW structures and is currently being used to generate forthcomming publications.

3.4 Evanescent Fields and Conjugate Matched Scatterers

An analysis is presented of k-space coupling of energy from an object into one or more proximal resonant scatterers. The choice of basis function provides insight into coupling mechanisms and efficiency which leads to the design of effective resonant scatterers that can direct energy and/or information associated with high-k evanescent fields away from the object. We discuss the trade-offs between the k-space and ω-space coupling as a function of the Q of the resonant scatterer. At the nanoscale, this has applications for super-Planckian heat removal as well as superresolution imaging.

One of the largest limitations to electronic, optoelectronic, and optical devices is the implicit generation of heat according to Joule's first law $\frac{dP}{dV} = \mathbf{J} \cdot \mathbf{E}$. Typically, heat is modeled as latent energy. However, this unrecoverable energy can simultaneously be viewed as incoherent infrared electromagnetic radiation that does not otherwise propagate away from

the heat source of interest. The notion of harvesting this otherwise wasted energy is the focus of the well established fields of thermophotovoltaics (TPVs) and thermoelectrics. At present, a number of automotive and industrial thermoelectric devices are on the market, demonstrating the importance of and interest in their continued research and development.

Separately, over the preceding ten years, some considerable attention has been devoted to the enhanced thermal radiative transfer which occurs when a hyperbolic metamaterial (HMM) is in extremely close proximity to a source of heat [26]. In fact, the power spectral density of a near-field coupled HMM has been shown to exceed Kirchoff's black body limit by several orders of magnitude as radiative transfer is inversely proportional to the separation distance between the HMM and hot body [64]. The super-Planckian thermal transfer associated with near field coupled HMMs is a direct result of the increased photonic density of states (PDOS) intrinsic to indefinite media with subwavelength periodicity [34]. The realization of devices utilizing this effect has been problematic, as the mechanical limitations of creating a stable, near-field-separated, thin film device are considerable. One proposed idea is a nanometer scale separation between two metallic layers. However, the combination of the Casimir force and thermal expansion can be expected to work against the intended effect of having an enhanced steady-state radiative thermal emission. Recently, the notion of increasing radiative transfer from an electrically large (on the order of the wavelength or larger) body such that it exceeds the black body limit has been posed [43]. In Tretyakov's seminal work, a rigorous derivation of radiative transfer as a function of spatial dimension and basis set is presented. Using [43] as a guide, practical cases of methods which theoretically show the potential for super-Planckian far field radiation are

examined.

The latent heat in a system can be modeled as a set of non-radiating electromagnetic modes. This concept was put forth by R.M. Rytov in 1967 whereby a formulation for radiative transfer in terms of Maxwell's equations was presented [39]. The critical contribution of this work is the development of the coherence theory for thermal fluctations. The knowledge of how the notion of extrapolating thermal fluctuations to circuit theory later appeared.

$$L_e(\nu, T, \sigma) = \frac{2h\nu^3}{c^2} \frac{\sigma}{e^{\frac{h\nu}{KbT}} - 1} \tag{36}$$

The Planck distribution (36), gives $L_e(\nu, T, \sigma)$, the power per unit frequency per unit area per steradian generated through spontaneous emission and is the product of Planck's quantum harmonic oscillator, a pre-factor which represents the number of modes per unit volume in a cavity, and the object's emissivity (σ), which is absolutely identical to its electromagnetic absorptivity [25]. Since absorption cannot exceed unity in practice, the black body which absorbs all light incident upon it is the perfect radiator. There exists, however, a potential exception to this theoretical limit. It is known in the radio frequency antenna community that the radar cross section of an antenna can be designed such that it exceeds the geometric cross section of the antenna itself [71]. The connection between radiative heat transfer and electromagnetism having been established, the question is then posed: what are the radiative properties of a thermal antenna with a radar cross section larger than its physical size?

The answer is theoretically approached by Maslovski et al[43] wherein the unique nature of an indefinitely sized spherical scatterer which could allow the body to exhibit a

non-reciprocal coupling to a source of heat is discussed. The requirement for this super-Planckian exchange is that the scatterer must be conjugately matched to the source of heat. It is significant to note that the proposed coupling takes place at distances on the order of the Mie size parameter $n \times k$. In this manner one does not implicitly minimize reflections at the boundary by satisfying (37)

$$\Gamma = \frac{Z_1 - Z_2}{Z_1 + Z_2} = 0 \tag{37}$$

but rather ensures a maximal electromagnetic coupling between two bodies. The electrodynamic formalism which relates the coupled system relies on using vector transmission line analysis (VTLA). VTLA provides a mathematically compact method for relating vectorial waves on a transmission line to vector spherical harmonics (VSH) in free space that emit from and converge to a spherical scatterer. A complete description of the derivation of the VTLA equations is presented elsewhere [70]. VTLA also naturally lends itself to the development of impedance boundary conditions in scenarios where the variation of the field quantities normal to the boundary vary linearly, providing (48) as a solution to Maxwell's equations for a time varying field of the form $e^{-j\omega t}$.

$$\nabla \times \mathbf{E} = j\omega\mu\mathbf{H} \qquad \nabla \times \mathbf{H} = -j\omega\varepsilon\mathbf{E} \tag{38}$$

$$\mathbf{E} = \mathbf{E}_\perp + \hat{\mathbf{n}}E_{||} \qquad \mathbf{H} = \mathbf{H}_\perp + \hat{\mathbf{n}}H_{||} \tag{39}$$

$$\mathbf{E}_\perp \cdot \hat{\mathbf{n}} = 0 \qquad \mathbf{H}_\perp \cdot \hat{\mathbf{n}} = 0 \qquad \mathbf{E}_{||} \cdot \hat{\mathbf{n}} = |\mathbf{E}_{||}| \qquad \mathbf{H}_{||} \cdot \hat{\mathbf{n}} = |\mathbf{H}_{||}| \tag{40}$$

$$\nabla = \nabla_\perp + \nabla_{||} \qquad \nabla_\perp = \frac{\partial}{\partial x}\hat{\mathbf{x}} + \frac{\partial}{\partial y}\hat{\mathbf{y}} \qquad \nabla_{||} = \frac{\partial}{\partial z}\hat{\mathbf{n}} \tag{41}$$

The strategy is to create a vector wave equation which contains no normal components of the fields which we wish to solve for.

$$\hat{\mathbf{n}}H_{||} = \frac{1}{j\omega\mu}\nabla_{\perp}\times\mathbf{E}_{\perp} \qquad\qquad \hat{\mathbf{n}}E_{||} = -\frac{1}{j\omega\varepsilon}\nabla_{\perp}\times\mathbf{H}_{\perp} \tag{42}$$

We then wish to find the transverse components of **E** and **H**. For both fields the transverse components are of the form:

$$\nabla_{\perp}\times\mathbf{E}_{||} + \nabla_{||}\times\mathbf{E}_{\perp} = \frac{\partial\mathbf{B}_{\perp}}{\partial t} \tag{43}$$

$$\frac{\partial}{\partial z}\times\mathbf{E}_{\perp} - \frac{1}{j\omega\varepsilon}\nabla_{\perp}\times(\nabla_{\perp}\times\mathbf{H}_{\perp}) = j\omega\mu\mathbf{H}_{\perp} \tag{44}$$

$$\frac{\partial}{\partial z}\times\mathbf{H}_{\perp} + \frac{1}{j\omega\mu}\nabla_{\perp}\times(\nabla_{\perp}\times\mathbf{E}_{\perp}) = -j\omega\varepsilon\mathbf{E}_{\perp} \tag{45}$$

Equations (44) and (45) are then transformed into vector transmission line equations by cross multiplying with $-\hat{\mathbf{n}}$. Upon transformation we obtain:

$$\frac{\partial}{\partial z}\mathbf{E}_{\perp} = \left(j\omega\mu\bar{\bar{I}}_{\perp} + \frac{j}{\omega\varepsilon}\nabla_{\perp}\nabla\perp\right)\cdot\left(\hat{\mathbf{n}}\times\mathbf{H}_{\perp}\right) \tag{46}$$

$$\frac{\partial}{\partial z}\hat{\mathbf{n}}\times\mathbf{H}_{\perp} = \left(j\omega\varepsilon\bar{\bar{I}}_{\perp} + \frac{j}{\omega\mu}\hat{\mathbf{n}}\times\nabla_{\perp}\hat{\mathbf{n}}\times\nabla_{\perp}\right)\cdot\mathbf{E}_{\perp} \tag{47}$$

From (46) and (47) we see the rightmost dotted terms which provide an analogy to the scalar transmission line equations, and thus produce a term which represents the induced current $(\hat{\mathbf{n}}\times\mathbf{H}_{\perp})$ as well as a term which represents the voltage $(\mathbf{E}_{\perp})$. The symbol $\bar{\bar{I}}_{\perp}$ denotes the transverse unit dyadic $(\hat{\mathbf{x}}\hat{\mathbf{x}}+\hat{\mathbf{y}}\hat{\mathbf{y}})$. Equation (48) then results from substituting (46) into (47) thus eliminating the term for the vector current.

$$\frac{\partial^2}{\partial z^2} + \left(\beta_{\mathrm{TM}}^2\frac{\mathbf{k}_{\perp}\mathbf{k}_{\perp}}{k_{\perp}^2} + \beta_{\mathrm{TE}}^2\frac{\mathbf{n}\times\mathbf{k}_{\perp}\mathbf{n}\times\mathbf{k}_{\perp}}{k_{\perp}^2}\right)\cdot\mathbf{E}_{\perp} = 0 \tag{48}$$

Having established impedance boundary conditions for a given system and developed a wave equation for our system of interest, the subsequent analysis of energy transfer can then be reduced to a T-matrix calculation.

The intent behind the development of the VTLA is to develop a formalism for a thermal source coupled to some type of scatterer. One potential scattering configuration is the use of negative index metamaterials as thermal antennae. The introduction of the 'perfect lens' by John Pendry [53] has led to a resurgence of interest in subwavelength electromagnetic devices in the literature. The fundamental premise behind the superresolution mechanism enabled by negative index materials is that subwavelength materials or structures are justifiably approximated as quasi-static. The quasi-static field approximation leads to an effective medium approximation with respect to the electrical permittivity of the material of interest since the material system being studied does not experience a significant spatial variation of the incident field [81]. The effective medium approximations for multi-layer thin film stacks wherein the uniaxial constituent layers have differing signs of permittivity and satisfy the relationship:

$$\varepsilon_{\perp} < 0\,,\, \varepsilon_{||} > 0 \; or \; \varepsilon_{\perp} > 0\,,\, \varepsilon_{||} < 0 \tag{49}$$

$$\frac{k_1^2 + k_2^2}{\varepsilon_{\perp}} + \frac{k_3^2}{\varepsilon_{||}} = k_o^2 \tag{50}$$

Considering the spatial dispersion of such a multi-layer structure one sees that the effective medium equations predict unbounded dispersion manifolds in reciprocal space. This prediction is known to be accurate within the limitation $ka \lesssim 1$. The condition for propagation across boundaries when an indefinite spatial dispersion profile is considered results in the continuity of the transverse wave vector across the boundary which simultaneously

satisfies the normal impedance conditions at the boundary of interest. Neglecting the magnetic response due to eddy currents, we note that $\mathbf{k} = \omega\sqrt{\varepsilon(\theta)\varepsilon_0\mu_0}$ and can then extend (49) to a generalized form for arbitary angles of incidence and uniaxial constituents, which frequently becomes necessary in the case of epitaxial material systems. This relationship is described by equation (20).

There are two conditions which allow for propagation through a material which satisfies the requirements of a hyperbolic metamaterial. The first, and most common, is to use diffractive optical components to couple transverse electromagnetic waves HMMs as previously discussed. The transverse momentum discrepancy between the propagating wave vectors in the HMM structure is then resolved by the grating's contribution to the wave's momentum which is shown in (51).

$$k_\perp = k_0 \sin(\theta) \pm \frac{2\pi \mathrm{n}}{\Lambda} \qquad n = 0, 1, 2... \tag{51}$$

Astute readers will notice that (51) provides a mechanism whereby the transverse momentum exceeds that of free space. Upon transitioning from a regime where $k_0 > k_\perp$ to $k_0 < k_\perp$ the diffracted orders become evanescent, and deliver no power to the surrounding environment unless they couple to another body. The other means by which one can couple a wave from free space to a HMM is through the careful selection of the constitutive materials which comprise the HMM [21]. Returning to the condition for propagation across the HMM boundary: continuity of the transverse wave vectors, one can then consider the properties of an HMM whose effective permittivity magnitude is less than that of free space. Typically reflection reaches a maximum as one increases the angle of incidence relative to the surface normal past the Brewster angle. However, in the case of a HMM with an

effective permittivity magnitude less than unity, reflection is minimized at glancing angles of incidence. This is a unique feature of HMMs and allows for the design of novel optical components which direct electromagnetic waves in a manner which is otherwise unattainable with passive components. This intrinsic endfire directivity is detailed elsewhere [22]. The final interesting feature of HMMs is the spatial independence on the photonic density of states.

The suggested mechanism from Sergei Tretyakov for out-coupling latent heat is the resonant scattering associated negative index materials. Since negative index materials exhibit time reversal symmetry breaking, the loss mechanisms then naturally transform themselves to conjugate matched impedances [51]. However, while the use of negative index metamaterials is sufficient to satisfy the requirements set forth to achieve super-Planckian radiative transfer, herein it is suggested negative index is by no means necessary for the desired effect. Excepting anomalous dispersion owed to strong absorption due to photon-phonon coupling, passive systems are well-described as having a capacative nature at frequencies associated with the majority of the radiative transfer from a given body. Thus, conjugate matching only requires an inductive response from our scatterer. The search for inductive response at infrared and optical frequencies led to a number of efforts in the area of nanofabrication centering around resonant elements such as split ring resonators or nanoscale lumped element inductors. The fundamental trade off in design is that these structures are extremely sensitive to fabrication tolerances and polarization of the incident wave. As the end goal is to have an easily constructed polarization independent device, these difficulties present a non-starter to many applications of interest.

The mechanism by which one can obtain a magnetic response at optical frequencies was described long ago by Landau and Lifshitz. Their predictions were revisited by Roberto Merlin [44] in the context of the magnetic resonances necessary to obtain truly negative index metamaterials. Fundamentally, magnetic resonances can be generated through geometric resonances which correspond to the field distributions of magnetic dipoles. A popular topology which readily demonstrates magnetic dipole resonances is that of a sphere. Following the analytic derivation of van der Hulst [32] for the field distributions scattered from spheres of arbitrary size, one can see that half the coefficients of the spherical wave expansion represent a magnetic response because spatially they are the curl of the electric dipole terms. Since the evanescent field exists in the volume of a HMM rather than exclusively at the surface, the statistical spatial correlation of thermal fluctuations in the HMM to the desired eigenmodes in the conjugate scatterer should in principle increase as the volumetric interaction implicitly has more spatial degrees of freedom for a given mode.

3.5 Transient Dynamics of Evanescent Fields

Some time after the perfect lens had been first presented by Pendry, Hegde et al turned their attention to a computational investigation of the dynamics of nanoscale superresolution imaging with the superlens [27]. Previous research immediately following the perfect lens concept discussed the potential mechanisms by which the system response became unphysical [24]. By studying the optical forces transferred by the perfect lens in a time-dependent scenario, one sees there is an implicit temporal dampening that is proportionate to the wave vector of interest. Thus, to obtain higher spatial resolution than typically obtained according to the diffraction limit, one must pay a price in time. With the result of

Gómez-Santos, Hegde et al presented a plot of image settling time vs wavevector showing that very high spatial frequencies could take days or even years to obtain. In the same work it was also shown that the temporal latency effects were dependent upon the thickness of the perfect lens. As the perfect lens' working distance is a function of its thickness, this effect further shows the limited use of such a device.

Returning to Maslovski et al [43], one can then consider how the temporal latency of negative index metamaterials relates to the maximal index of the VSH summation. Since the number of VSHs that contribute to the super-Planckian radiative transfer for spheres is directly related to the loss tangent of the emitter, low-loss negative index metamaterials can contribute as many as a hundred spectral terms to the far field radiation from a conjugate matched scatterer. It remains, then, to evaluate what the minimum rate of emission must be for a VSH to couple in real time such that the individual harmonic reproduces the same result as the steady state solution.

A mechanism to test the limits of radiative thermal transfer has been proposed. It seems that there may exist some special cases wherein steady state solutions provide for a violation of Kirchoff's black body limit. However, in practice, the implicit temporal latency of high-k states should limit the ability to demonstrate the effects of metamaterial superemitters that rely upon negative index electrodynamic phenomena [43].

CHAPTER 4: ALUMINIUM ZINC OXIDE

4.1 Introduction to Aluminium Zinc Oxide

At present, various seemingly disconnected fields of research have serendipitously pursued the development of transparent crystalline thin films made of aluminium zinc oxide (AZO) for a host of applications. AZO is currently one of the most popular alternatives to indium tin oxide (ITO), as it frees one from the concerns associated with the indium supply chain. The panel display community continues to look for transparent electronics with optical and electronic properties equal to or better than ITO to create thin film transistors [16]. Meanwhile, the plasmonics and metamaterial communities continue the search for efficient visible and near infrared wavelength plasmonic materials to improve sensing, beam steering, and sub-wavelength imaging [78, 47, 66].

Recently, Eastman-Kodak has made significant progress in developing high speed spatially selective atomic layer deposition technology (SALD). By selectively depositing atomic layers over a given surface one can achieve a design pattern by simply printing the desired footprint. Using patterned-by-printing materials thus eliminates the need for lithographic techniques to produce structures which have the properties and geometries required by the designer [14]. In order to predict the behavior/response of these hybrid structures their intrinsic properties must be well understood. This can be somewhat problematic as the degrees of freedom presented by the process parameters can create some ambiguity in un-

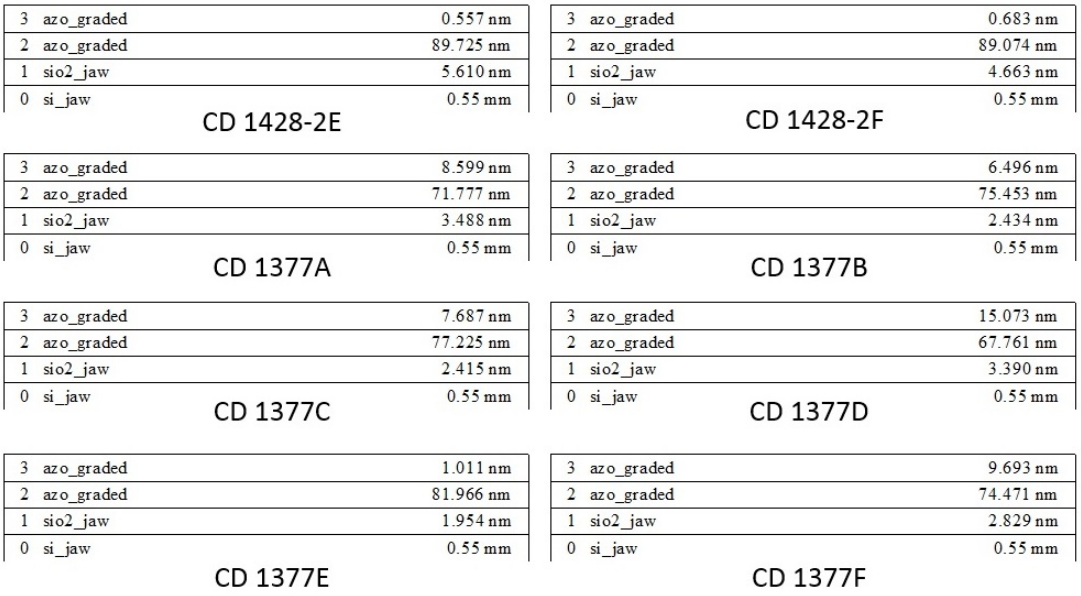

Figure 29: WVASE32 Model Geometries depicting the 4-layer model used to characterize SALD AZO samples grown at 250°C on silicon. Notice the inclusion of silicon dioxide at the silicon substrate interface as well as the two layers required to describe AZO rather than a single material layer.

derstanding the optical response of the material. The characterization of these films is further complicated by the presence of an ensemble of shallow energy level donor states. As even unintentionally doped ZnO demonstrates conductivity gradients [57], evaluating ternary ZnO systems to obtain of the infrared optical response can be expected to be a more complex task .

It is known that long wave sensing, i.e. IR and THz, offers greater sensitivity to certain quantities of interest such as conductivity and carrier mobility [61, 29]. At the same time certain spectral features are constrained by optical activity that can only be detected in the visible to ultraviolet [40]. In the process of developing oscillator models which describe the absorptive phenomena of a crystalline material measured by variable angle spectroscopic ellipsometry (VASE), it is conventionally thought that free electrons, phonons, band

gap transitions, and polariton states are the sole sources of dispersion. However, as can be seen from numerous sources [4, 76, 69, 59] aluminium zinc oxide crystal systems exhibit shallow absorption features whose energies cannot be ascribed to the previously mentioned phenomena. In the past this discrepancy has typically been resolved by the use of non-causal extended Drude models. The semiempirical extended Drude model is shown in Eq. 52 and Eq. 53. The well known form of 52 is augmented by a functional form of the scattering term such that ω_τ is parameterized by $\omega_{\tau 0}$, the low frequency scattering rate, ω_{tr}, the scattering transition frequency, ω_{tl}, the past-transition scattering rate, α, the power law dependence, and σ, the broadening term. In Fig. 30 we show how such models are of limited use when compared to a spectrally well-resolved broadband characterization of a transparent conducting oxide by VASE. Thanks to the work of Kim et al [77] a Hubbard-U model which corrects the density of states in AZO for non-local interaction is now available.

The Hubbard-U correction arises out of a failure of density functional theory to predict the behavior of Mott insulators [11], which are materials that are predicted to be conductors but instead act as insulators. This discrepancy arises out of correlated electron interaction of free carriers due to interatomic forces in a crystalline lattice. This effect and many other relevant phenomena are discussed in much greater detail in [74]. As such, we are herein able to illustrate the connection between non-local response, extended Drude models, and the incompletely described shallow absorption states in AZO.

$$\varepsilon(\omega) = -\frac{\omega_p^2}{\omega^2 + i\omega\omega_\tau} \tag{52}$$

$$\omega_\tau(\omega) = \frac{\omega_{\tau 0}}{1 + e^{\frac{\omega-\omega_{tr}}{\sigma}}} + \left(1 - \frac{1}{1 + e^{\frac{\omega-\omega_{tr}}{\sigma}}}\right)\omega_{\tau l}\left(\frac{\omega}{\omega_{tr}}\right)^{\alpha} \tag{53}$$

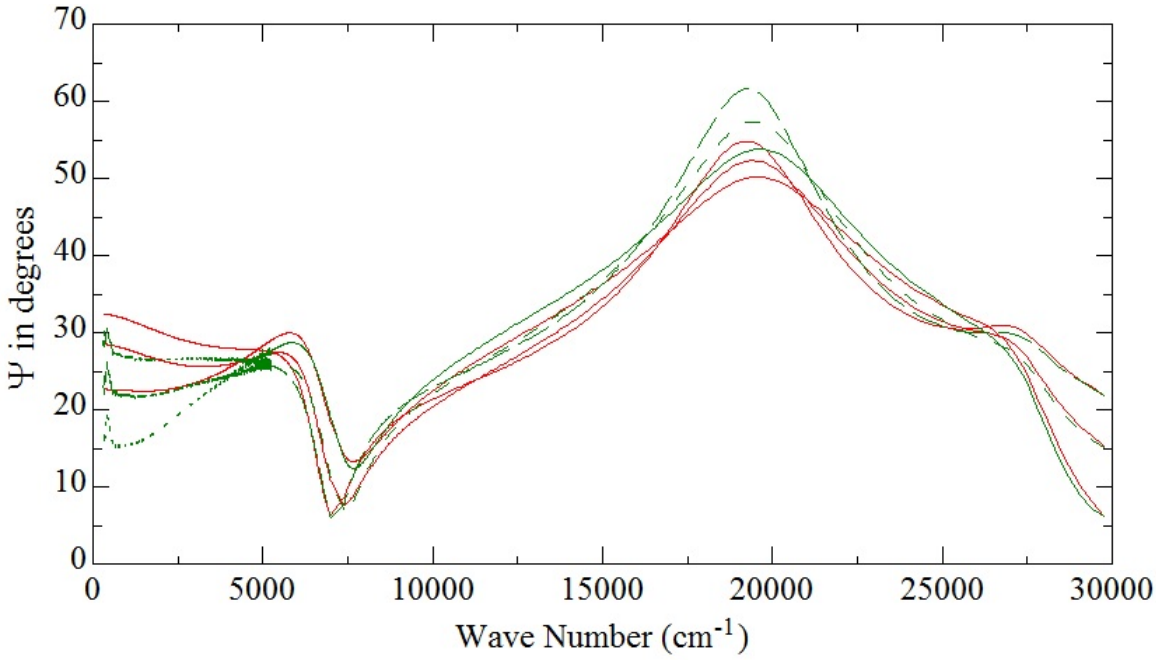

Figure 30: Experimental data (dashed green) vs extended Drude model (solid red) for three angles of incidence.

One of the most important process parameters in ALD is the substrate temperature during deposition. As SALD is essentially metal organic chemical vapor deposition with a printer head, the necessary energy to de-ligandize the precursors must still come from thermalization. For this reason, the large number of samples (54) are grouped by their growth temperature and substrate type to simplify the comparisons. In this work, only samples grown at 250°C on silicon are discussed. Both the latent heat as well as the mass flow of a given precursor ratio are observed to strongly affect the morphology of AZO thin films [12, 42]. This has been studied in some detail [83, 7] but not extensively for SALD. SALD seems to exhibit lower resistivity than typical ALD AZO [79, 13]. The high conductivity of SALD films further exaggerates the discrepancies between IR VASE measurements and extended Drude models used to fit reflection and transmission from FTIR data. It also presents a lower time cost in both production and device development as devices can be di-

rectly written with differing form factors. These salient features make SALD AZO a prime candidate for investigation via broadband spectroscopic ellipsometry. There is no readily available infrared ellipsometric data for SALD films. As such herein we present broadband ellipsometric characterization from 300 to 30,000 cm^{-1}

4.2 Ellipsometry Data and Fitting for AZO

Many of the existing works regarding the optical properties of transparent conducting oxides such as AZO and ITO combine spectroscopic ellipsometry over the visible to near infrared spectral range with a FTIR measurement in the mid-to-far IR [79, 38] to capture the spectral response associated with free carrier absorption. As previously mentioned, in a covalently bonded solid absorption phenomena can be attributed to free carriers, inter sub band transitions, inter band transitions, phonons, and polariton states. Due to the mixed characteristic nature of their bonds, transparent conducting oxides exhibit some of the traits of a covalently bonded solid as well as those of an ionic compound [15]. As such, the ionized donor states in zinc oxide do not produce classical free electron behavior as one might expect. This is due to the fact that in a ZnO crystal lattice aluminium may replace either zinc or oxygen substitutionally or be incorporated as an interstitial lattice inclusion. The aluminium substitution for zinc may occur for one, two, or three aluminium atoms, leading to a spread of energy states according to [77]. It remains to be determined how the growth process parameters contribute to the individual populations of these inclusions to the total ensemble of states. Due to the relatively broad energy spread of these states combined with their shallow absorption relative to the free carrier population as well as their proximity to the intrinsic Drude resonance, they are almost impossible to spectrally resolve

without variable angle spectroscopic ellipsometry. More specifically, FTIR reflection and transmission data is inedaquate for the task at hand.

Table 3: GenOsc parameters for 250°C samples. The Drude response is captured by ρ, the resistivity and τ, the scattering rate. E_{Tauc} represents the onset of indirect transitions associated with phonon absorption while E_n represents the energy associated with the direct inter band transition. A, E, and Br are the amplitude, center energy, and broadening of Gaussian absorption features. Notice the absense of a definite exciton peak in the imaginary part of the permittivity as shown in Tab. 6. The lack of a sharp narrow peak following the indirect transitions gives clear evidence of non-excitonic shallow donor states.

Sample	$\rho, \tau(fs)$	A, E, Br	A, E, Br	A, E, Br	A, E, Br	E_{Tauc}, E_n
1428-2E	0.0011 , 5.7	27 , 332 , 4139	65 , 388 , 109	8.35 , 714 , 1797	0.59 , 5061 , 3762	3.14 , 3.6
1428-2F	0.00087 , 5.8	24 , 313 , 4895	61 , 391 , 108	12 , 853 , 108	0.3 , 5913 , 3466	2.99 , 3.95
1377A	0.0011 , 4.9	- , - , -	65 , 383 , 135	14 , 605 , 5893	12 , 863 , 2620	3.21 , 3.84
1377B	0.00082 , 4.6	- , - , -	75 , 365 , 164	15 , 1017 , 2651	5 , 1206 , 5910	3.1 , 4.01
1377C	0.00086 , 4.3	- , - , -	67 , 368 , 166	16 , 709 , 2872	5 , 1456 , 5618	3.17 , 4.39
1377D	0.00092 , 5.4	- , - , -	47 , 399 , 124	19 , 633 , 2658	6 , 1786 , 5742	3.24 , 4.92
1377E	0.001 , 3.9	- , - , -	73 , 358 , 168	10 , 832 , 2974	4 , 1742 , 5392	3.24 , 3.93
1377F	0.00098 , 5.1	- , - , -	52 , 395 , 107	23 , 511 , 3164	5 , 1185 , 5843	3.15 , 3.84

In order to provide an accurate yet understandable model for the optical response of AZO from experimental ellipsometric data, we use J.A. Woollam Company's WVASE32 software. The model geometry as shown consists of the standard definition silicon substrate, native silicon dioxide, AZO, and a surface layer which only contains a Drude term, a pole, and a ε_1 offset. The AZO and surface layers are modeled using the GenOsc layer in WVASE32. Initially experimental data sets are converted into point-by-point fits in order to obtain a reference absorption spectrum. From this reference, Kramers-Kronig consistent oscillator responses are applied such that a causal best-fit dielectric function is obtained. The necessary model geometry parameters are presented in Fig. 29. The primary motivation of this analysis is on the bulk response of the material. Present in the model geometry used for the 250°C set of samples on silicon substrates is a surface layer which accounts for surface charge gradients. It is thought that this surface layer should also possess an

Table 4: Reflectance polarization ratio (Ψ) for three angles of incidence (65°, 70°, 75°) for 250°C AZO samples. Dashed green lines indicate experimental data. Red line indicates calculated oscillator model parameters.

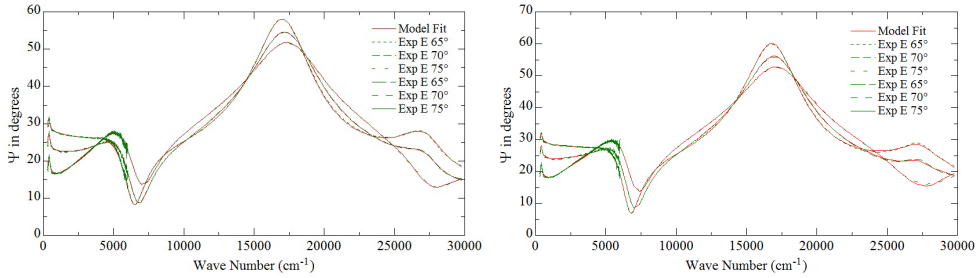

(a) CD 1428-2E

(b) CD 1428-2F

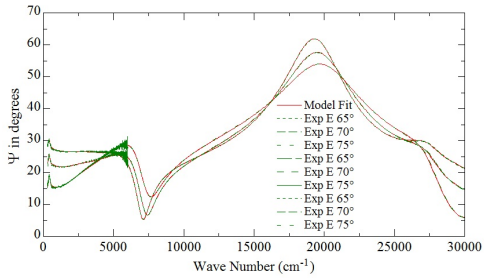

(c) CD 1377A

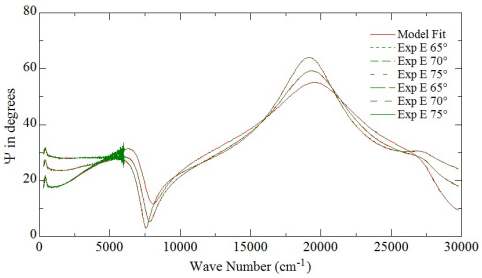

(d) CD 1377B

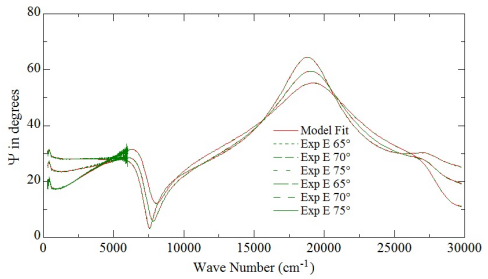

(e) CD 1377C

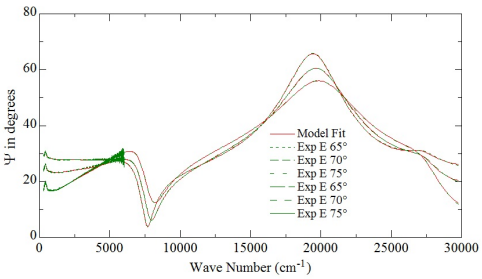

(f) CD 1377D

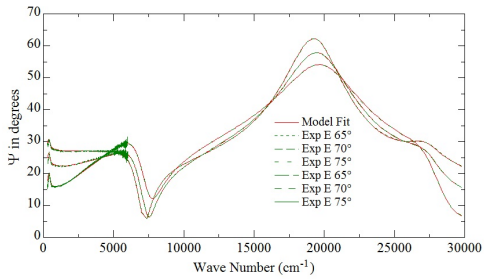

(g) CD 1377E

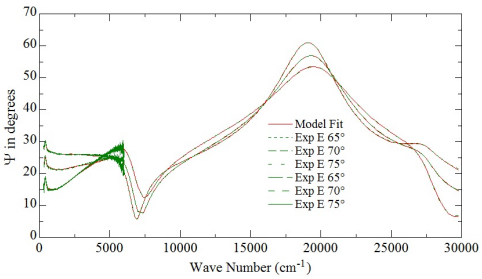

(h) CD 1377F

oscillator which transitions through the deep UV, however such experimental data is not readily available, and so the spectal range is limited to approximately 250 nm or 5 eV. As such, a pole is used to account for the interband transitions which occur beyond the range of the experimental data. This is standard practice as taught by J.A. Woollam Co. in their WVASE32 short course.

The oscillator model for AZO consists of a Drude term (ρ, τ), Gaussian oscillators to capture both a phonon peak which occurs between approximately 350 to 390 cm^{-1} seen in Tab.4 as well as the shallow donor states which are the primary concern of this work, and lastly, a Tauc-Lorentz oscillator to capture the effect of the inter band transitions associated with a direct band gap semiconductor which are evident in Tab.5. It should be noted that the Tauc-Lorentz oscillator is typically used for amorphous materials such as ITO and that J.A. Woollam does provide a series of PSEMI oscillator models whose line shapes better capture the effects of semiconductor materials with a more definite crystalline character. The comparisons of the relative accuracy of the Tauc-Lorentz vs the PSEMI oscillator models show a slight (negligible) difference in mean square error and so are not discussed for the sake of brevity. Samples 1428-2E and 1428-2F also have an additional Gaussian oscillator to compensate for an extra shallow energy level donor state which only appears in samples which are believed to be doped rather than alloyed due to their significantly lower aluminium content. This implies the primary inclusion mechanism is subsitution of oxygen by aluminium for lower volume fractions of aluminium. The discrepancies between doping and alloying relate to the previous discussion of the inclusion mechanisms of aluminium into the zinc oxide crystalline system.

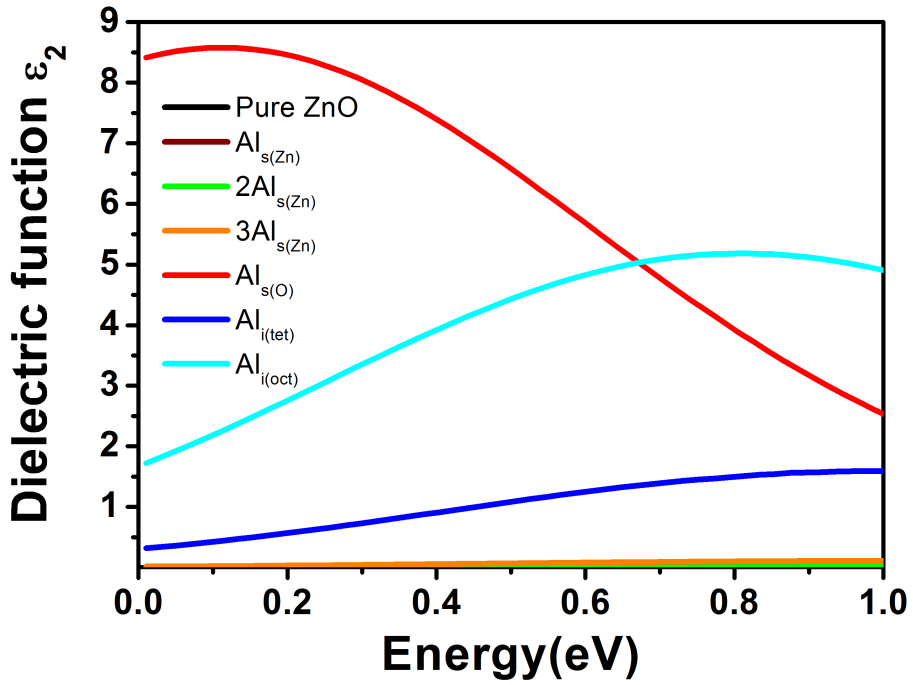

Figure 31: Scaled figure with data kindly provided by the authors of [77] showing the theoretically calculated energy levels of the different absorption mechanisms in AZO crystalline systems.

Again returning to [77] one sees that the most free carrier-like absorption feature associated with a specific inclusion mechanism is that of aluminium substituted for oxygen. However, as one increases the Al fraction relative to stoichiometric ZnO, one statistically increases the occurence of the other inclusion schemes. This leads to the presence of shallow donor states which begin to contribute to the thermally ionized carrier population at room temperature due to the Burstein-Moss shift, and otherwise complicates the spectroscopic analysis necessary to understand the optical properties of the films. However, by using first principle calculations and wideband VASE measurements, we can obtain a precise and accurate result which allows us to predictively design using AZO. It must be emphasized that the most conductive films are not those with the highest content of aluminium.

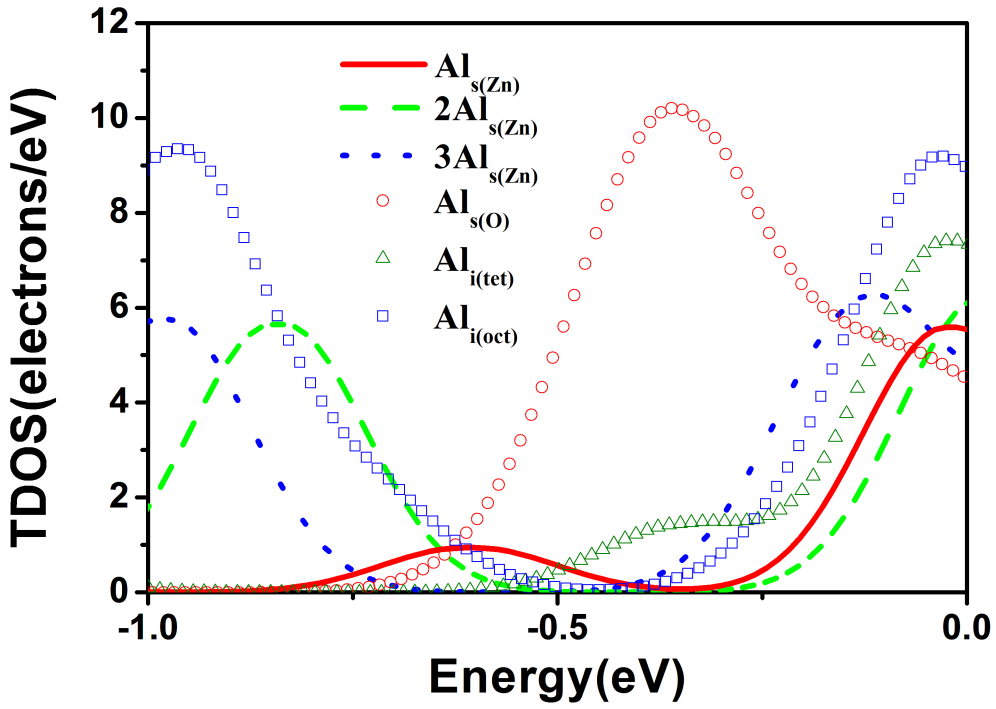

Figure 32: Total Density of States plot kindly provided by the authors of [77]. The rightmost x-axis value (0 eV) corresponds to the Fermi level. As the Fermi level is pushed higher and higher into the conduction band according to the Burstein-Moss effect more of the states associated with the various inclusion mechanisms are brough into the conduction band.

Examination of Fig. 31 reveals that the electronic density of states within a few tenths of eV (hundreds of wavenumbers) of the Fermi level does not have a linear dependence on energy. To be clear, as the various inclusion mechanisms contribute to the free carrier concentration and move the Fermi level further towards and subsequently into the conduction band, one has to use the product of the Maxwell-Boltzman distribution with the density of states shown in Fig. 32 to obtain the relative contribution of each inclusion mechanism due to the overlap of the different states with the available thermal energy. This non-linear correspondence between the volume fraction of aluminium and the free carrier population is an archetypal of the fundamental difference between doping and alloying as well as the great

difficulty encountered by spectroscopists working with transparent conducting oxides.

The combination of Gaussian oscillators and the standard covalent absorption mechanisms coupled with careful analysis is sufficient to produce the dielectric functions shown in Tab. 6. All the models show a striking similarity to the experimental data so much so that they are virtually indistinguishable and have a mean squared error of less than 2. This very good agreement between the model presented and the experimental data is sufficient to be sure that the values are correct within the limits prescribed by the software designers. The last remaining step in fully characterizing the films consists of removing all the poles from the oscillator models presented in Fig. 29 by measuring the effects of interband transitions that approach the vacuum ultraviolet spectral range (VUV). The VUV data will be necessary to resolve drastically shifted Fermi levels due to extremely high carrier concentrations which cause interband transitions that occur above energies of 5.5 eV. These shifted interband transitions also tend to correlate with the lower energy transitions associated with the bulk of the material relative to the surface layer leading to some difficulty in spectrally resolving them from neighboring transitions.

In conclusion, we have determined that the wideband VASE measurement of thin film transparent conducting oxides leads to superior knowledge of and confidence in the determined optical properties thereof. Without the work of density functional theorists using novel methods to correct for non-local contributions to the electronic density of states, this result would be impossible to obtain. The author cannot help but note that the knowledge of both VASE measurement and DFT produces a synnergistic understanding of an extremely complex problem, reinforcing the validity of interdisciplinary research method-

ologies. While the analysis presented is not ultimately complete, it is sufficient for the purposes of industry to understand the correlation between optical and electrical measurements to within a nominal error. As such, the methods presented in this section will provide a path going forward for other researchers working to better understand the optical and electronic properties of transparent conducting oxides.

Table 5: Relative optical path difference (Δ) for three angles of incidence (65°, 70°, 75°) for 250°C AZO samples. Dashed green lines indicate experimental data. Red line indicates calculated oscillator model parameters.

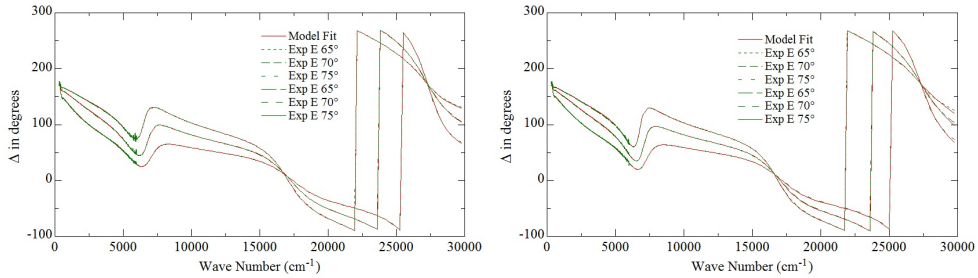

(a) CD 1428-2E

(b) CD 1428-2F

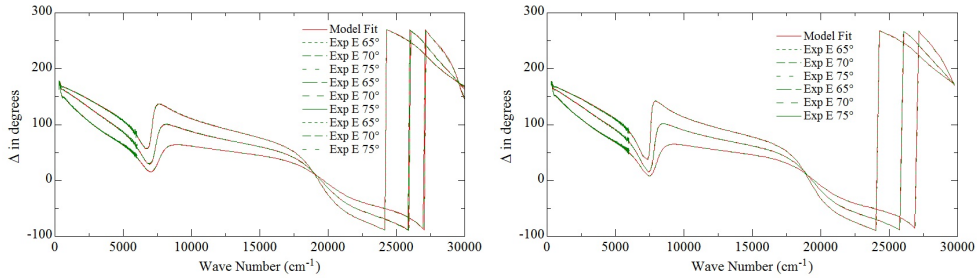

(c) CD 1377A

(d) CD 1377B

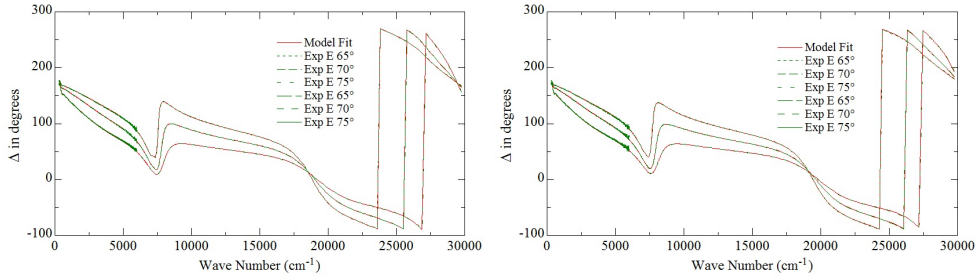

(e) CD 1377C

(f) CD 1377D

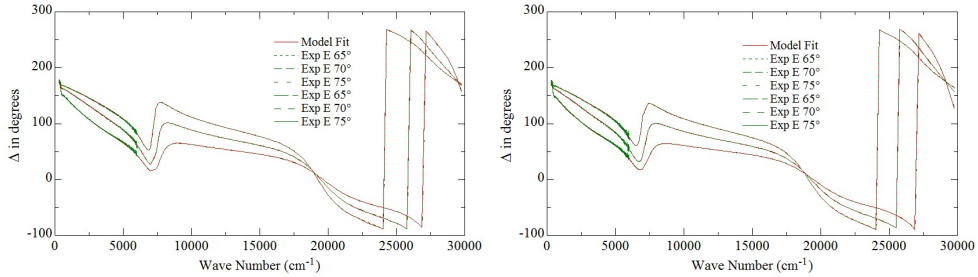

(g) CD 1377E

(h) CD 1377F

Table 6: Real and Imaginary (log scale) relative permittivities for 250°C AZO samples. Red lines indicate the real part ε_1 while the dashed green lines indicate the imaginary part ε_2.

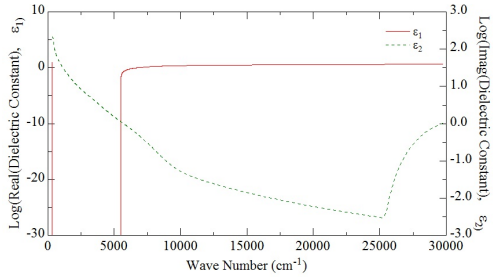

(a) CD 1428-2E

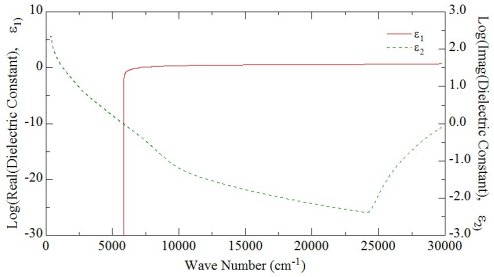

(b) CD 1428-2F

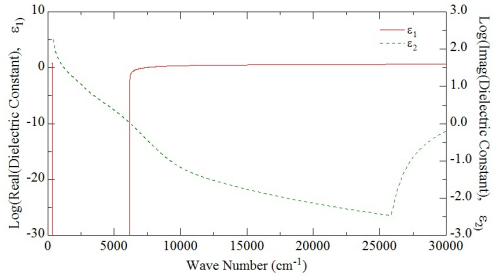

(c) CD 1377A

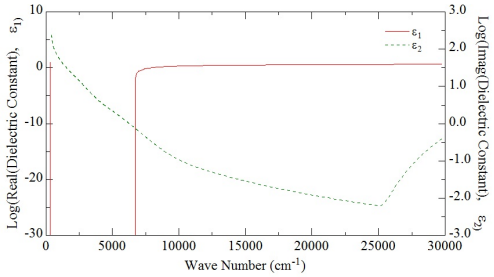

(d) CD 1377B

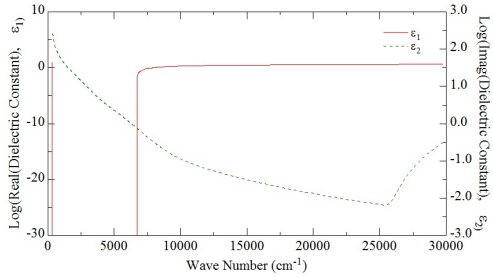

(e) CD 1377C

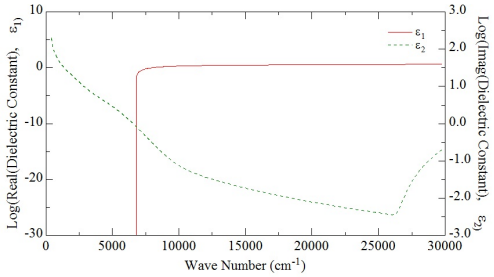

(f) CD 1377D

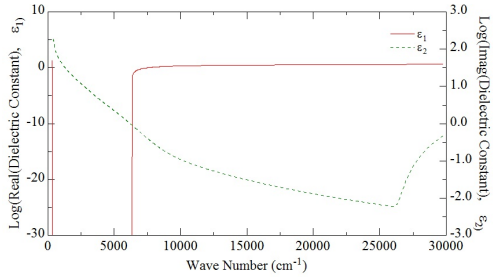

(g) CD 1377E

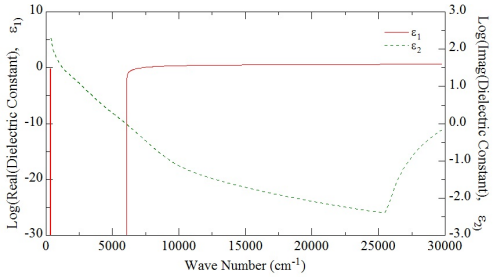

(h) CD 1377F

CHAPTER 5: SUMMARY

In this section I would like to provide a clear statement of my individual contribution to the work presented herein and the conlusions reached there from. Initially, I had to learn the operation and maintenance of Professor Raphael Tsu's III-V nitride molecular beam epitaxy (MBE) system. This requires detailed knowledge of proper substrate cleaning, as well as delicate mechanical skills. Great care is also required, as one simultaneously uses liquid nitrogen, components that can hold temperatures of over 1000°C, and floating voltages on components such as the reflection high energy electron diffraction apparatus which can spontaneously discharge onto a careless user. After learning how to run and service the MBE I then had to determine the best method to obtain a doped zinc oxide film. I found that the three possible candidates for n-type doping of ZnO are aluminium, gallium, and indium. After researching the different proceedures associated with each material, I chose to attempt to use a Knudsen effusion cell for the simultaneous co-evaporation of both zinc and aluminium in an oxygen plasma environment. The sublimation of zinc proved to be ineffective in our system and so I made the choice to improvise by using an electron beam to vaporize zinc. In addition, concerns over the coefficient of thermal expansion of aluminium led me to use gallium as an n-type dopant. After some trial and error, two different samples of gallium zinc oxide were obtained.

After growing the first two samples, I then dedicated my efforts to characterization. The films were measured by numerous methods enumerated in section 3.1. The X-ray and ellipsometry analysis gave evidence of reasonable quality polycrystalline films. I then began my two summers working at A*STAR in Singapore with Dr. Ravi Hegde. I was tasked with using finite element analysis to reproduce the optical response of the two gallium doped zinc oxide HMMs I had produced by MBE. After a considerable amount of iteration, a Kramers-Kronig consistent dispersion relation was obtained giving a very good agreement with the measured data. I then simulated the effects of different k-vectors being incident on the gallium zinc oxide HMM structure. The result of running hundreds of simulations with different grating periods and frequencies is the dispersion plot shown in Fig. 21. I produced this 3D plot by tabulating all the simulation data and plotting as a function of grating period and temporal frequency.

I then turned my attention to the installation and operation of the Nanoscribe Photonic Professional GT. Utilizing the Nanoscribe system requires knowledge of the creation of .stl files or else some scripting to direct the laser beam path. The user must then choose how to render the object into machine code by using Nanoscribe's DeScribe software. The DeScribe output is then loaded into NanoWrite, the actual operational software for the Nanoscribe system. Both DeScribe and NanoWrite have a large number of parameters and features, all of which have some contribution to the speed and quality of the resulting structure. Having found a reasonable range of parameters, I was able to begin printing gratings, spheres, split ring resonators, and more for the purposes of creating a library of various scattering structures to study both in conjunction with HMMs and as stand alone objects.

A significant number of simulations were performed on standing split ring resonators made of only dielectric, but no strong absorption features were ever determined. As I wished to both simulate and fabricate structures prepared by 3D direct laser writing, I realized that I would need to know the dielectric response of the constituent materials used in the Nanoscribe system.

It was at this point that I was serendipitiously introduced to Professor Tino Hofmann, who had independently realized the importance of characterizing the monomers used in the Nanoscribe system. I then created a method to obtain thin (less than 10 micron) films of IP-Dip and IP-L, the Nanoscribe monomers, such that the infrared VASE could sufficiently resolve the absorption features of the monomers without being overwhelmed by Fabry-Perot oscillations. I then measured both films and created models to describe their dispersion profile. After iterating with Professor Hofmann, I was able to obtain a very good agreement between my model and my experimental data such that the discrepancies between the two were unnoticable by eye.

I was also tasked with an investigation into a series of aluminium zinc oxide thin films prepared by Carolyn Ellinger of the Eastman-Kodak company per Professor Fiddy's request. Attempts to synthesize aluminium zinc oxide had led to a number of questions about the properties of various phases of aluminium, zinc, and oxygen. One question that remained to be answered from previous work was, "How much aluminium can you try to incorporate into zinc oxide before each aluminium no longer contributes one free electron to the lattice?". Initially, I chose to characterize the Kodak samples on the UV-Vis VASE. This provided me with data from 350 nm to 2 μm. There were some uncertainties as to

the effects of the doping level on the infrared optical properties of the AZO which led me to measure the samples again on the IR-VASE. I then chose to combine the two spectral regimes into one data set which led to a broadband characterization effort.

I then created an optical model for AZO which had absorption features which could not be ascribed to phonons, Drude response, inter band transitions, or some more exotic light-matter coupling (polariton states). It was suggested that such a model was not feasible and that some other explanation would be required to justify our model to colleagues in our field. However, recalling many conversations with Professor Raphael Tsu regarding both covalent and ionic bonding radii, I remembered that the presumptive absorption schemes previously mentioned were functions of a purely covalently bound solid, which zinc oxide is assuredly not. Using some intuition, I was able to find a very recent paper on the density functional theory of AZO. This paper was essential to understanding the optical response that I was measuring as well as justifying my model for the absorption phenomena in AZO. The key result of [77] is that the density of states below the Fermi level in AZO is non-linear as a function of the various inclusion mechanisms. This shows that the increase of aluminium does not generate a linear dependence on the free carrier concentration, our desired result.

Because of the Kramers-Kronig relations, the value of the real part of the dispersion relation at any single frequency depends on some contribution of the imaginary part at all frequencies. This led to the observation by Professor Hofmann that trying to simultaneously evaluate the infrared and visible spectral range might produce inconsistent results. This observation was in fact correct. I was able to overcome the difficulty imposed by the

bandwidth of the data set by enforcing a uniform ε_1 offset for the two layers of the geometry which represent the optical behavior of AZO. This simple realization combined with the standard practices taught by J.A. Woollam allowed me to successfully characterize the subset of samples I was asked to study, thus concluding my course of research.

REFERENCES

[1] V. Agranovich and V. Kravtsov. Notes on crystal optics of superlattices. *Solid State Communications*, 55(1):85–90, 1985.

[2] F. Aieta, P. Genevet, M. A. Kats, N. Yu, R. Blanchard, Z. Gaburro, and F. Capasso. Aberration-free ultrathin flat lenses and axicons at telecom wavelengths based on plasmonic metasurfaces. *Nano letters*, 12(9):4932–4936, 2012.

[3] J. Bauer, A. Schroer, R. Schwaiger, and O. Kraft. Approaching theoretical strength in glassy carbon nanolattices. *Nat. Mater.*, 5:438–443, 2016.

[4] A. Bingel, K. Füchsel, N. Kaiser, and A. Tünnermann. Zno: Al films prepared by inline dc magnetron sputtering. *Advanced Optical Technologies*, 3(1):103–111, 2014.

[5] L. Brillouin. Wave guides for slow waves. *J. Appl. Phys.*, 19:1023, 1948.

[6] T. Bückmann, N. Stenger, M. Kadic, J. Kaschke, A. Frölich, T. Kennerknecht, C. Eberl, M. Thiel, and M. Wegener. Tailored 3d mechanical metamaterials made by dip-in direct-laser-writing optical lithography. *Adv. Mater.*, 24(20):2710–2714, 2012.

[7] A. A. Chaaya, R. Viter, I. Baleviciute, M. Bechelany, A. Ramanavicius, Z. Gertnere, D. Erts, V. Smyntyna, and P. Miele. Tuning optical properties of al2o3/zno nanolaminates synthesized by atomic layer deposition. *The Journal of Physical Chemistry C*, 118(7):3811–3819, 2014.

[8] G. Chen. Thermal conductivity and ballistic-phonon transport in the cross-plane direction of superlattices. *Physical Review B*, 57(23):14958, 1998.

[9] E. L. Chu and W. W. Hansen. The theory of disk-loaded wave guides. *Journal of Applied Physics*, 18.11:996–1008, 1947.

[10] J. W. Cleary, M. Snure, K. D. Leedy, D. C. Look, K. Eyink, and A. Tiwari. Mid-to long-wavelength infrared surface plasmon properties in doped zinc oxides. In *SPIE Security+ Defence*, pages 854504–854504. International Society for Optics and Photonics, 2012.

[11] M. Cococcioni and S. De Gironcoli. Linear response approach to the calculation of the effective interaction parameters in the lda+ u method. *Physical Review B*, 71(3):035105, 2005.

[12] T. Dhakal, D. Vanhart, R. Christian, A. Nandur, A. Sharma, and C. R. Westgate. Growth morphology and electrical/optical properties of al-doped zno thin films grown by atomic layer deposition. *Journal of Vacuum Science & Technology A*, 30(2):021202, 2012.

[13] C. R. Ellinger and S. F. Nelson. Selective area spatial atomic layer deposition of zno, al2o3, and aluminum-doped zno using poly (vinyl pyrrolidone). *Chemistry of Materials*, 26(4):1514–1522, 2014.

[14] C. R. Ellinger and S. F. Nelson. Design freedom in multilayer thin-film devices. *ACS applied materials & interfaces*, 7(8):4675–4684, 2015.

[15] Z. Fan and J. G. Lu. Zinc oxide nanostructures: synthesis and properties. *Journal of nanoscience and nanotechnology*, 5(10):1561–1573, 2005.

[16] E. Fortunato, D. Ginley, H. Hosono, and D. C. Paine. Transparent conducting oxides for photovoltaics. *MRS bulletin*, 32(03):242–247, 2007.

[17] A. M. Fox. *Optical properties of solids*, volume 3. Oxford university press, 2001.

[18] D. Franklin, Y. Chen, A. Vazquez-Guardado, S. Modak, J. Boroumand, D. Xu, S.-T. Wu, and D. Chanda. Polarization-independent actively tunable colour generation on imprinted plasmonic surfaces. *Nat. Comm.*, 6:7337, 2015.

[19] H. Fujiwara. *Spectroscopic ellipsometry: principles and applications*. John Wiley & Sons, 2007.

[20] D. Fullager, H. Alisafaee, R. Tsu, and M. Fiddy. Epitaxial thin films for hyperbolic metamaterials. In *SPIE OPTO*, pages 899515–899515. International Society for Optics and Photonics, 2014.

[21] D. Fullager, H. Alisafaee, R. Tsu, and M. Fiddy. Epitaxial thin films for hyperbolic metamaterials. In *SPIE OPTO*, pages 899515–899515. International Society for Optics and Photonics, 2014.

[22] D. B. Fullager and M. A. Fiddy. Design theory of thin film hyperbolic metamaterial colimators. In *SPIE Nanoscience+ Engineering*, pages 95441T–95441T. International Society for Optics and Photonics, 2015.

[23] T. Galfsky, E. Narimanov, and V. Menon. Enhanced spontaneous emission in photonic hypercrystals. In *Frontiers in Optics*, pages FW6A–3. Optical Society of America, 2015.

[24] G. Gomez-Santos. Universal features of the time evolution of evanescent modes in a left-handed perfect lens. *Physical review letters*, 90(7):077401, 2003.

[25] J.-J. Greffet and M. Nieto-Vesperinas. Field theory for generalized bidirectional reflectivity: derivation of helmholtzs reciprocity principle and kirchhoffs law. *JOSA A*, 15(10):2735–2744, 1998.

[26] Y. Guo, C. L. Cortes, S. Molesky, and Z. Jacob. Broadband super-planckian thermal emission from hyperbolic metamaterials. *Applied Physics Letters*, 101(13):131106, 2012.

[27] R. S. Hegde, Z. Szabo, Y. L. Hor, Y. Kiasat, E. P. Li, and W. J. Hoefer. The dynamics of nanoscale superresolution imaging with the superlens. *IEEE Transactions on Microwave Theory and Techniques*, 59(10):2612–2623, 2011.

[28] R. S. e. a. Hegde. The dynamics of nanoscale superresolution imaging with the superlens. *Microwave Theory and Techniques, IEEE Transactions*, 59.10:2612–2623, 2011.

[29] C. M. Herzinger, M. M. Schubert, T. Hofmann, M. M. Liphardt, and J. A. Woollam. Terahertz-infrared ellipsometer system, and method of use, 2015. US Patent 9,041,927.

[30] J. Hu, X. Zhao, R. Li, A. Zhu, L. Chen, Y. Lin, B. Cao, X. Zhu, and C. Wang. Broadband circularly polarizing dichroism with high efficient plasmonic helical surface. *Opt. Express*, 24(10):11023–11032, May 2016.

[31] Z. Huang and E. E. Narimanov. Veselago lens by photonic hyper-crystals. *Applied Physics Letters*, 105(3):031101, 2014.

[32] H. C. Hulst and H. C. van de Hulst. *Light scattering by small particles*. Courier Corporation, 1957.

[33] L. V. A. E. N. Jacob, Zubin. Optical hyperlens: far-field imaging beyond the diffraction limit. *Optics Express*, 14.18:8247–8256, 2006.

[34] Z. Jacob. Engineering vacuum and thermal fluctuations using hyperbolic metamaterials. *Session 3P3b 2 FocusSession. SC2: Plasmonics in the Quantum Regime 2*, page 1138.

[35] Z. Jacob, L. V. Alekseyev, and E. Narimanov. Semiclassical theory of the hyperlens. *JOSA A*, 24(10):A52–A59, 2007.

[36] Z. Jacob, J.-Y. Kim, G. Naik, A. Boltasseva, E. Narimanov, and V. Shalaev. Engineering photonic density of states using metamaterials. *Applied physics B*, 100(1):215–218, 2010.

[37] A. V. Kildishev and E. E. Narimanov. Impedance-matched hyperlens. *Optics letters*, 32(23):3432–3434, 2007.

[38] H. C. Knoops, B. W. van de Loo, S. Smit, M. V. Ponomarev, J.-W. Weber, K. Sharma, W. M. Kessels, and M. Creatore. Optical modeling of plasma-deposited zno films: Electron scattering at different length scales. *Journal of Vacuum Science & Technology A: Vacuum, Surfaces, and Films*, 33(2):021509, 2015.

[39] M. L. Levin and S. Rytov. Theory of equilibrium thermal fluctuations in electrodynamics, 1967.

[40] S.-G. Lim, S. Kriventsov, T. N. Jackson, J. Haeni, D. Schlom, A. Balbashov, R. Uecker, P. Reiche, J. Freeouf, and G. Lucovsky. Dielectric functions and optical bandgaps of high-k dielectrics for metal-oxide-semiconductor field-effect transistors by far ultraviolet spectroscopic ellipsometry. *Journal of applied physics*, 91(7):4500–4505, 2002.

[41] N. Lindenmann, G. Balthasar, D. Hillerkuss, R. Schmogrow, M. Jordan, J. Leuthold, W. Freude, and C. Koos. Photonic wire bonding: a novel concept for chip-scale interconnects. *Opt. Express*, 20(16):17667–17677, 2012.

[42] W. Maeng, J.-w. Lee, J. H. Lee, K.-B. Chung, and J.-S. Park. Studies on optical, structural and electrical properties of atomic layer deposited al-doped zno thin films with various al concentrations and deposition temperatures. *Journal of Physics D: Applied Physics*, 44(44):445305, 2011.

[43] S. I. Maslovski, C. R. Simovski, and S. A. Tretyakov. Overcoming black body radiation limit in free space: metamaterial superemitter. *New Journal of Physics*, 18(1):013034, 2016.

[44] R. Merlin. Metamaterials and the landau–lifshitz permeability argument: large permittivity begets high-frequency magnetism. *Proceedings of the National Academy of Sciences*, 106(6):1693–1698, 2009.

[45] R. Merlin, C. Colvard, M. Klein, H. Morkoc, A. Cho, and A. Gossard. Raman scattering in superlattices: Anisotropy of polar phonons. *Applied Physics Letters*, 36(1):43–45, 1980.

[46] H. Morkoç and Ü. Özgür. *Zinc oxide: fundamentals, materials and device technology*. John Wiley & Sons, 2008.

[47] G. V. Naik, J. Liu, A. V. Kildishev, V. M. Shalaev, and A. Boltasseva. Demonstration of al: Zno as a plasmonic component for near-infrared metamaterials. *Proceedings of the National Academy of Sciences*, 109(23):8834–8838, 2012.

[48] Nanoscribe. "application examples, http://www.nanoscribe.de/en", 2016. accessed 2016/11/21.

[49] E. E. Narimanov. Photonic hypercrystals. *Physical Review X*, 4(4):041014, 2014.

[50] A. Niv, G. Biener, V. Kleiner, and E. Hasman. Manipulation of the pancharatnam phase in vectorial vortices. *Optics express*, 14(10):4208–4220, 2006.

[51] J. Pendry. Time reversal and negative refraction. *Science*, 322(5898):71–73, 2008.

[52] J. B. Pendry. Negative refraction makes a perfect lens. *Physical Review Letters*, 85.18:3966, 2000.

[53] J. B. Pendry. Negative refraction makes a perfect lens. *Physical review letters*, 85(18):3966, 2000.

[54] J. B. e. a. Pendry. Magnetism from conductors and enhyanced nonlinear phenomena. *Microwave Theory and Techniques, IEEE Transactions*, 47.11:2075–2084, 1999.

[55] S. Peng, R. Zhang, V. H. Chen, E. T. Khabiboulline, P. Braun, and H. A. Atwater. Three-dimensional single gyroid photonic crystals with a mid-infrared bandgap. *ACS Photon.*, 3(6):1131–1137, 2016.

[56] A. Poddubny, I. Iorsh, P. Belov, and Y. Kivshar. Hyperbolic metamaterials. *Nature Photonics*, 7(12):948–957, 2013.

[57] K. Sago, H. Kuramochi, H. Iigusa, K. Utsumi, and H. Fujiwara. Ellipsometry characterization of polycrystalline zno layers with the modeling of carrier concentration gradient: Effects of grain boundary, humidity, and surface texture. *Journal of Applied Physics*, 115(13):133505, 2014.

[58] B. E. Saleh, M. C. Teich, and B. E. Saleh. *Fundamentals of photonics*, volume 22. Wiley New York, 1991.

[59] J. Sap, O. Isabella, K. Jäger, and M. Zeman. Extraction of optical properties of flat and surface-textured transparent conductive oxide films in a broad wavelength range. *Thin Solid Films*, 520(3):1096–1101, 2011.

[60] M. Schröder, M. Bülters, C. von Kopylow, and R. Bergmann. Novel concept for three-dimensional polymer waveguides for optical on-chip interconnects. *J. Europ. Opt. Soc. Rap.*, 7(0):12027, 2012.

[61] M. Schubert, P. Kühne, V. Darakchieva, and T. Hofmann. Optical hall effectmodel description: tutorial. *JOSA A*, 33(8):1553–1568, 2016.

[62] D. Schurig and D. R. Smith. Spatial filtering using media with indefinite permittivity and permeability tensors. *Applied Physics Letters*, 82(14):2215–2217, 2003.

[63] N. Shitrit, S. Maayani, D. Veksler, V. Kleiner, and E. Hasman. Rashba-type plasmonic metasurface. *Optics letters*, 38(21):4358–4361, 2013.

[64] C. Simovski, S. Maslovski, I. Nefedov, S. Kosulnikov, P. Belov, and S. Tretyakov. Hyperlens makes thermal emission strongly super-planckian. *Photonics and Nanostructures-Fundamentals and Applications*, 13:31–41, 2015.

[65] D. R. Smith, D. Schurig, J. J. Mock, P. Kolinko, and P. Rye. Partial focusing of radiation by a slab of indefinite media. *Applied Physics Letters*, 84(13):2244–2246, 2004.

[66] C. M. Soukoulis, T. Koschny, P. Tassin, N.-H. Shen, and B. Dastmalchi. What is a good conductor for metamaterials or plasmonics. *Nanophotonics*, 4(1), 2015.

[67] R. Synowicki and T. E. Tiwald. Optical properties of bulk c-ZrO_2, c-MgO and a-As_2S_3 determined by variable angle spectroscopic ellipsometry. *Thin Solid Films*, 455:248–255, 2004.

[68] H. G. Tompkins, T. Tiwald, C. Bungay, and A. E. Hooper. Use of molecular vibrations to analyze very thin films with infrared ellipsometry. *J. Phys. Chem. B*, 108(12):3777–3780, 2004.

[69] R. Treharne, K. Hutchings, D. Lamb, S. Irvine, D. Lane, and K. Durose. Combinatorial optimization of al-doped zno films for thin-film photovoltaics. *Journal of Physics D: Applied Physics*, 45(33):335102, 2012.

[70] S. Tretyakov. *Analytical modeling in applied electromagnetics*. Artech House, 2003.

[71] S. Tretyakov. Maximizing absorption and scattering by dipole particles. *Plasmonics*, 9(4):935–944, 2014.

[72] M. I. Tribelsky, J.-M. Geffrin, A. Litman, C. Eyraud, and F. Moreno. Small dielectric spheres with high refractive index as new multifunctional elements for optical devices. *Scientific reports*, 5:12288, 2015.

[73] M. I. Tribelsky, J.-M. Geffrin, A. Litman, C. Eyraud, and F. Moreno. Directional fano resonances in light scattering by a high refractive index dielectric sphere. *Physical Review B*, 94(12):121110, 2016.

[74] R. Tsu. *Superlattice to nanoelectronics*. Elsevier, 2005.

[75] V. G. Veselago. The electrodynamics of substances with simultaneously negative values of epsilon and mu. *Physics-Uspekhi*, 10.4:509–514, 1968.

[76] N. Wolf, D. Gerstenlauer, and J. Manara. Modelling the spectral reflectances of miscellaneous ito coatings by using only the drude theory. In *Journal of Physics: Conference Series*, volume 395, page 012064. IOP Publishing, 2012.

[77] H.-C. Wu, H.-H. Chen, and Y.-R. Zhu. Effects of al-impurity type on formation energy, crystal structure, electronic structure, and optical properties of zno by using density functional theory and the hubbard-u method. *Materials*, 9(8):647, 2016.

[78] M.-R. Wu, J.-R. C. Chien, C.-J. Wu, and S.-J. Chang. Near-infrared multichannel filter in a finite semiconductor metamaterial photonic crystal. *IEEE Photonics Journal*, 8(1):1–9, 2016.

[79] Y. Wu, P. Hermkens, B. Van de Loo, H. Knoops, S. Potts, M. Verheijen, F. Roozeboom, and W. Kessels. Electrical transport and al doping efficiency in nanoscale zno films prepared by atomic layer deposition. *Journal of Applied Physics*, 114(2):024308, 2013.

[80] T. Xu and H. J. Lezec. Visible-frequency asymmetric transmission devices incorporating a hyperbolic metamaterial. *Nature communications*, 5, 2014.

[81] J. Yu. Self-consistent evaluation of complex constitutive parameters. *IEEE Transactions on Antennas and Propagation*, 29(2):408–412, 1981.

[82] S. Yushanov, L. Gritter, J. Crompton, and K. Koppenhoefer. Surface plasmon resonance. In *COMSOL Conference*, 2012.

[83] C.-H. Zhai, R.-J. Zhang, X. Chen, Y.-X. Zheng, S.-Y. Wang, J. Liu, N. Dai, and L.-Y. Chen. Effects of al doping on the properties of zno thin films deposited by atomic layer deposition. *Nanoscale Research Letters*, 11(1):407, 2016.

[84] N. I. Zheludev. What diffraction limit? *Nature Materials*, 7.6:420–422, 2008.